

**Comprehensive analysis of chromatin states in atypical teratoid/rhabdoid tumor identifies diverging roles for SWI/SNF and Polycomb in gene regulation**

Serap Erkek<sup>1,2,3,4\*</sup>, Pascal D. Johann<sup>1,2,5\*</sup>, Martina A. Finetti<sup>6\*</sup>, Yiannis Drosos<sup>7</sup>, Hsien-Chao Chou<sup>7</sup>, Marc Zapatka<sup>8</sup>, Dominik Sturm<sup>1,2,5</sup>, David T.W. Jones<sup>1,2</sup>, Andrey Korshunov<sup>9,10</sup>, Marina Rhyzova<sup>11</sup>, Stephan Wolf<sup>12</sup>, Jan-Philipp Mallm<sup>13,14</sup>, Katja Beck<sup>14</sup>, Olaf Witt<sup>5,15</sup>, Andreas E. Kulozik<sup>5</sup>, Michael C. Frühwald<sup>16,17</sup>, Paul A. Northcott<sup>1,2,18</sup>, Jan O. Korbel<sup>3</sup>, Peter Lichter<sup>8,14</sup>, Roland Eils<sup>13,19</sup>, Amar Gajjar<sup>7</sup>, Charles W.M. Roberts<sup>7</sup>, Daniel Williamson<sup>6</sup>, Martin Hasselblatt<sup>20</sup>, Lukas Chavez<sup>1,2#</sup>, Stefan M. Pfister<sup>1,2,5#</sup>, Marcel Kool<sup>1,2#+</sup>

<sup>1</sup>Hopp-Children's Cancer Center at the NCT Heidelberg (KITZ), Heidelberg, Germany.

<sup>2</sup>Division of Pediatric Neurooncology, German Cancer Research Center (DKFZ) and German Cancer Consortium (DKTK), Heidelberg, Germany.

<sup>3</sup>European Molecular Biology Laboratory, Genome Biology Unit, Heidelberg, Germany.

<sup>4</sup>Izmir Biomedicine and Genome Center, Izmir, Turkey

<sup>5</sup>Department of Pediatric Hematology and Oncology, University Hospital Heidelberg, Germany.

<sup>6</sup>Wolfson Childhood Cancer Research Centre, Northern Institute for Cancer Research, Newcastle University, Newcastle Upon Tyne, United Kingdom.

<sup>7</sup>Department of Oncology, St Jude Children's Research Hospital, Memphis, USA.

<sup>8</sup>Division of Molecular Genetics, German Cancer Research Center (DKFZ) and German Cancer Consortium (DKTK), Heidelberg, Germany.

<sup>9</sup>Department of Neuropathology, University Hospital Heidelberg, Germany.

<sup>10</sup>Clinical Cooperation Unit Neuropathology, German Cancer Research Center (DKFZ), Heidelberg, Germany.

<sup>11</sup>Department of Neuropathology, Burdenko Neurosurgical Institute, Moscow, Russia.

<sup>12</sup>Genomics and Proteomics Core Facility, German Cancer Research Center (DKFZ), Heidelberg, Germany.

<sup>13</sup>Genome Organization & Function Research Group, German Cancer Research Center (DKFZ), Heidelberg, Germany.

<sup>14</sup>Heidelberg Center for Personalized Oncology, DKFZ-HIPO, DKFZ, Heidelberg, Germany.

<sup>15</sup>Clinical Cooperation Unit Pediatric Oncology, German Cancer Research Center (DKFZ), Heidelberg, Germany.

<sup>16</sup>University Children's Hospital Augsburg, Swabian Children's Cancer Center, Germany.

<sup>17</sup>EU-RHAB registry Center, Augsburg, Germany.

<sup>18</sup>Department of Developmental Neurobiology, St. Jude Children's Research Hospital, Memphis, TN, USA.

<sup>19</sup>Division of Theoretical Bioinformatics, German Cancer Research Center (DKFZ), Heidelberg, Germany.

<sup>20</sup>Institute of Neuropathology, University Hospital Münster, Germany.

\* These authors are co-first authors

# These authors are co-senior authors

+ lead contact

Manuscript correspondence:

**Marcel Kool, Ph.D.**

Deputy Division Head and Group leader, Division of Pediatric Neurooncology

German Cancer Research Center (DKFZ)

Im Neuenheimer Feld 280

D-69120 Heidelberg, Germany

[m.kool@kitz-heidelberg.de](mailto:m.kool@kitz-heidelberg.de)

+49.6221.42 4636 (P)

+49.6221.42 4639 (F)

## **RUNNING TITLE**

The chromatin landscape of atypical teratoid rhabdoid tumors

## **SUMMARY**

Biallelic inactivation of *SMARCB1*, encoding a member of the SWI/SNF chromatin remodeling complex, is the hallmark genetic aberration of atypical teratoid rhabdoid tumors (ATRT). Here, we report how loss of *SMARCB1* affects the epigenome in these tumors. Using ChIP-sequencing on primary tumors for a series of active and repressive histone marks, we identified the chromatin states differentially represented in ATRTs compared to other brain tumors and non-neoplastic brain. Re-expression of *SMARCB1* in ATRT cell lines enabled confirmation of our genome-wide findings for the chromatin states. Additional generation of ChIP-seq data for SWI/SNF and Polycomb group proteins and the transcriptional repressor protein REST determined differential dependencies of SWI/SNF and Polycomb complexes in regulation of diverse gene sets in ATRTs.

## **SIGNIFICANCE**

Global loss of H3K27ac-associated chromatin states in ATRTs, compared to non-neoplastic tissue and other brain tumors, is not compensated by a global increase of repressive marks. Instead, H3K27me3 enrichment, strongly correlated with binding of EZH2 and REST, is mostly restricted to *SMARCB1* binding sites, resulting in repression of neuronal differentiation genes. A substantial fraction of

SMARCB1 binding sites in ATRTs is bound by EZH2 but lacks H3K27me3. Residual SWI/SNF complex binding, measured by SMARCA4 ChIP-seq, maintains these genes in an active state, even in the presence of Polycomb complex and REST. This divergent interplay between SWI/SNF and Polycomb hints at novel potential vulnerabilities in this dreadful disease, but also provides insights into fine-tuned regulatory networks relevant beyond ATRT biology.

## HIGHLIGHTS

- ATRT epigenomes display a global depletion of H3K27ac and H3K27me3
- Neuronal genes bound by SMARCB1 in normal brain are repressed by EZH2 in ATRT
- ATRT harbor many active genes occupied by EZH2 but without occupancy of H3K27me3
- Residual SWI/SNF occupancy maintains genes active in the presence of Polycomb

## INTRODUCTION

SWI/SNF complexes are chromatin remodelers consisting of multiple subunits, which mobilize nucleosomes (Kadoch et al., 2016). Approximately twenty percent of all human cancers have been shown to have mutations in one of the subunits of SWI/SNF complex (Kadoch et al., 2013). One of the subunits of SWI/SNF complex, SMARCB1 (also known as *SNF5*, *BAF47*, or *INI1*), is biallelically inactivated in roughly 95% of all malignant rhabdoid tumors (MRT). This is a group of highly aggressive tumors, which is seen in infants and young children mainly in kidney (rhabdoid tumor of the kidney - RTK), brain (atypical teratoid rhabdoid tumor - ATRT) and to a smaller extent in soft tissue and liver (Masliah-Planchon et al., 2015). In about 5% of MRT cases an inactivating mutation of SMARCA4 and not SMARCB1 is found, resulting presumably in the same consequence, which is the inactivation of the SWI/SNF complex (Hasselblatt et al., 2014; Schneppenheim et al., 2010). Recent studies characterizing the genomic landscape of ATRTs and extra-cranial MRTs reported stable genomes and inactivation of SMARCB1 largely by structural aberrations in the analyzed cases (Chun et al., 2016; Johann et al., 2016; Torchia et al., 2016).

Atypical teratoid rhabdoid tumors are highly malignant tumors of the central nervous system mainly seen in children younger than three years old and recognized as the most frequent malignant brain tumor in children younger than six months (Biswas et al., 2016). ATRT patients have a very poor prognosis with a median survival of around 17 months and existing therapy options mainly consist of chemotherapy and radiation. Although new therapeutic approaches – such as interference with EZH2 activity – are being developed, specificity and safety of these new therapy options need to be further studied (Ginn and Gajjar, 2012). Recent genomic studies characterizing ATRTs (Johann et al., 2016; Torchia et al., 2016) provided fundamental insights into molecular characteristics of this deadly disease. Importantly, we previously showed that ATRT consists of three molecular subgroups, termed ATRT-TYR, ATRT-SHH and ATRT-MYC, each characterized by distinct pathways aberrantly regulated (Johann et al., 2016). However, a comprehensive epigenetic characterization of the ATRT epigenome with respect to the loss of SMARCB1 has not been attempted in any of these recent landmark studies.

Over the last few years studies performed by ENCODE, Roadmap and IHEC projects investigated the epigenomic landscape of diverse non-pathogenic tissue/cell types and a few cancer cell lines by profiling histone modifications with active and repressive characteristics and integrating with transcriptomic and methylome data sets (Encode Project Consortium, 2012; Roadmap Epigenomics Consortium et al., 2015; Stunnenberg et al., 2016). The results of these studies gave important hints about chromatin organization in mostly physiological cell types. Given the high rate of dysregulation of chromatin modifiers in cancer (Brien et al., 2016) and the large discrepancy between cancer cell lines and primary cancers (Lin et al., 2016), studies characterizing chromatin landscapes of primary tumors are needed for complete molecular characterization of diverse tumors. Within the context of rhabdoid tumors, recent studies have shed more light on the function of SMARCB1 binding at enhancer elements (Johann et al., 2016; Torchia et al., 2016; Wang et al., 2017), but other global and

focal effects of SMARCB1 loss on the epigenome remain understudied. Despite being known as the genetic hallmark in rhabdoid tumors for more than two decades, there is still much unknown how loss of SMARCB1 drives ATRT tumorigenesis. A better understanding of the molecular mechanisms behind this is urgently needed in order to develop novel treatment strategies for patients with rhabdoid tumors who still face a very poor outcome (Fruhwald et al., 2016). Therefore, to assess the effect of SMARCB1 loss on the global distribution of histone modifications and chromatin states, we performed chromatin immunoprecipitation for six different types of histone modifications followed by sequencing (ChIP-seq) in 11 primary ATRT representing all three recently identified molecular subgroups (5 ATRT-TYR, 3 ATRT-SHH, 3 ATRT-MYC) (Johann et al., 2016) (Table S1) and identified chromatin states specifically represented in ATRTs. Further, integration of histone modification data with chromatin modifier localizations enabled the discovery that residual SWI/SNF activity is present in ATRT at genes important for tumorigenesis where it keeps these genes active despite the presence of the repressor EZH2.

## RESULTS

### *The chromatin landscape of ATRT*

Histone modifications associated with active chromatin organization and gene transcription (H3K27ac, H3K4me1, H3K4me3, H3K36me3) as well as gene repression (H3K27me3, H3K9me3) were analyzed, together representing the six core histone marks as analyzed by the IHEC, Roadmap, and ENCODE consortia (Encode Project Consortium, 2012; Roadmap Epigenomics Consortium et al., 2015; Stunnenberg et al., 2016). ATRT data were compared to corresponding sets of ChIP-Seq data generated for medulloblastoma (MB; n = 23), pediatric glioblastoma (pGBM; n = 3), pediatric normal brain (PNB; n = 1), and published data (Roadmap Epigenomics Consortium et al., 2015) for adult normal brain (ANB; n = 7) and embryonic stem cells (ESC; n = 5). To segment individual genomes into functionally distinct chromatin states, we applied the Roadmap 18-state chromatin segmentation model using chromHMM (Ernst and Kellis, 2012) (Figure 1A).

Quantification of the relative genomic fractions assigned to the 18 different chromatin states in ATRTs and other tissues showed that active enhancer states defined by co-occupancy of H3K27ac and H3K4me1 (e.g. EnhA1) and actively transcribed states defined by H3K36me3 (e.g. Tx), were significantly ( $p < 0.05$ ) underrepresented in ATRTs as compared to other pediatric brain tumors and PNB (Figure 1B-1C). The active promoter state (TssA, defined by H3K4me3 and H3K27ac) was also globally depleted in ATRTs compared to PNB and ANB, but was similarly represented in other brain tumors (Figure 1D). The relative fraction of the active flanking transcription start site downstream (TssFlnkD) state defined by H3K4me1 and H3K4me3 but lacking H3K27ac, was however significantly increased in ATRTs when compared with most other tissues (Figure 1E). These observations imply a selective loss of only H3K27ac-associated active states rather than a reduction of all active chromatin states in ATRT.

Surprisingly, however, the global loss of H3K27ac-associated active states in ATRTs was not compensated by a global increase in repressive states. Instead, repressed polycomb states (e.g. ReprPC) defined exclusively by H3K27me3, were largely depleted from ATRT genomes, especially when compared to PNB and other brain tumors (Figure 1F). Furthermore, we observed an overrepresentation of the quiescent state in ATRTs, which is devoid of any of the six histone marks covering ~70% of the genome (Figure 1G). In line with the embryonal origin of ATRTs (Pfister et al., 2010), the relative fractions of most chromatin states were overall rather similar to ESC (Figure S1A). Analyzing chromatin states for each of the three molecular subgroups of ATRTs separately revealed clear differences in the chromatin states of previously described subgroup-specific signature genes (Johann et al., 2016), for instance *CCND1*, *FOXK1* or *HOXC* (Figure 1H). We did not, however, observe major differences in genome-wide relative fractions of the different chromatin states between ATRT subgroups compared with other tissue types (Figure S1A), suggesting that SMARCB1 loss results in a

global depletion of H3K27ac and H3K27me3 marks, which was confirmed by quantitative comparisons and mass spectrometry analyses as well (Figure S1B-S1F).

Because of the unexpected global depletion of the H3K27me3-associated ReprPC state in ATRT we were interested in understanding to which chromatin states such genetic regions have switched. Most frequently, regions annotated as ReprPC states in PNB switched in ATRT to a quiescent state or to a weakly repressed Polycomb state (ReprPCWk) characterized by low H3K27me3 abundance (Figure S2A-S2B). When integrating DNA methylation data, genomic regions annotated as ReprPC in PNB and switching to different states in ATRT show significantly higher DNA methylation levels in ATRT compared with regions that remain in ReprPC state in ATRTs (Figure S2C), suggesting replacement of Polycomb-mediated repression of genomic regions in PNB by DNA methylation in ATRT.

#### *Re-expression of SMARCB1 in ATRT cell lines results in global gain of H3K27ac*

To validate the epigenetic changes observed in primary tumors caused by SMARCB1 loss, we re-expressed *SMARCB1* in two ATRT cell lines, BT12 and BT16, via transducing the cells with lentivirus expressing *SMARCB1* (Figure 2A). Immunoblotting confirmed expression of SMARCB1 protein in both BT12 and BT16 at physiological levels (Figure S3A). In line with previous observations (Ae et al., 2002; Betz et al, 2002), we saw a substantial reduction of the cell density after re-expression of *SMARCB1* for both cell lines as measured by bioluminescence (Figure S3B), caused by an early G1 cell cycle arrest and cellular senescence, followed by apoptosis (Figure S3C-S3F).

Next, we performed H3K27me3 and H3K27ac ChIP-seq on BT12 and BT16 cell lines before and after *SMARCB1* re-expression. In both cell lines, *SMARCB1* re-expression resulted in a substantial increase of regions with higher H3K27ac occupancy compared with the parental cell line lacking SMARCB1 (Figure 2B-2C). In BT16 cells, we also found an increase in H3K27me3, which was, however, less

pronounced in BT12 cells (Figure S3G-S3H). Mass spectrometry analyses measuring H3K27ac and H3K27me3 levels before and after SMARCB1 re-expression confirmed these increased levels of H3K27ac and H3K27me3 (Figure S3I). The great majority of regions gaining H3K27ac were promoter-distal as compared to regions losing H3K27ac (Figure 2D-2E), consistent with recent studies showing enrichment of the SWI/SNF complex at TSS-distal regions after SMARCB1 re-expression (Wang et al., 2017). Notably, 80% of the genomic regions gaining H3K27ac in BT12 overlapped the genomic regions gaining H3K27ac in BT16 (Figure 2F-2G), suggesting for a mechanistic baseline guiding *de novo* deposition of H3K27ac after re-expression of *SMARCB1*. Further, regions that gained H3K27ac in both cell lines were significantly enriched for H3K27ac-defined chromatin states in PNB as compared to ATRT (Fisher's exact test p value < 2.2e-16 and odds ratio=3.7). These results argue that *SMARCB1* re-expression induces a remodeling of chromatin states towards the distribution observed in normal pediatric brain tissue.

We performed RNA-seq to identify differentially expressed genes after SMARCB1 re-expression in BT12 and BT16 cell lines. Downregulated genes were mainly involved in stress response and metabolism while upregulated genes included many genes involved in neuron development such as *UNC5C*, *NDRG1* and *NEDD4L* (Figure S3J). Furthermore, we observed a positive correlation ( $\rho=0.59$ ) between changes in gene expression and changes in H3K27ac levels at genes upregulated after SMARCB1 re-expression (Figure 2H). Overall, these data re-emphasize the anti-proliferative functions of SMARCB1 but more importantly validate the findings of a global H3K27ac and H3K27me3 reduction in primary tissue.

#### *Chromatin landscape at SMARCB1 binding sites in ATRT*

Although several studies investigated the pathways deregulated upon SMARCB1 depletion in *in vitro* models (Johann et al., 2016; Kim and Roberts, 2014; Torchia et al., 2016; Wang et al., 2017; Wilson et al., 2010), the changes that occur in chromatin organization at SMARCB1 bound-genomic regions



after SMARCB1 loss are unknown. Therefore, beyond the global effects of SMARCB1 loss on the ATRT epigenome (Figure 1), we were specifically interested in epigenetic alterations at genomic regions in ATRTs that are bound by SMARCB1 in non-neoplastic tissue. Thus, we generated SMARCB1 ChIP-seq data in PNB and compared the representation of chromatin states in PNB and ATRTs at SMARCB1 binding sites. Similar to what has been observed on a genome-wide level, our analysis revealed a reduced representation of active chromatin states, especially of active enhancer states, and increased representation of quiescent chromatin states in ATRT compared to PNB at SMARCB1 binding sites (Figure 3A). However, in contrast to the genome-wide findings, Polycomb-mediated repressed chromatin states were enriched in ATRT in regions bound by SMARCB1 in PNB (Figure 3A), without major differences between ATRT subgroups (Figure S4A). These results demonstrate for the first time at a genome-wide scale the transition from active to repressed chromatin organization at SMARCB1 binding sites in primary tumors.

A more detailed analysis of promoters bound by SMARCB1 in PNB and characterized by a repressed chromatin state in ATRTs showed that regions surrounding the TSS indeed were specifically depleted for H3K27ac and gained H3K27me3 (Figure 3B). This is in line with the classical hypothesis that SMARCB1 depletion results in gain of H3K27me3 at specific gene loci. Expression levels of these genes were significantly lower in ATRT compared to PNB (Figure S4B). Pathway analysis revealed a significant enrichment of transcription factors involved in neuronal differentiation such as NEUROD2, EN2 and LHX1, and known tumor suppressor genes (TSGs) (Zhao et al., 2013) such as WNK2 (Figure 3C, Figure S4C-S4D) that appear to be repressed through this mechanism in ATRT. These results are fully in agreement with previous studies showing defects in neuronal differentiation in the absence of SMARCB1 in murine cell lines (Albanese et al., 2006) and repression of lineage specific genes in SMARCB1-deficient cell lines (Wilson et al., 2010) and further serve as a reference guide of SMARCB1-targeted yet repressed genes in a primary tumor deficient for SMARCB1 (Table S2).

### **SMARCB1-occupied genes are mainly silenced by EZH2**

The histone methyltransferase EZH2, part of the Polycomb repressive complex 2 (PRC2), is responsible for establishing most H3K27me3 marks in the genome and has been described as an important epigenetic modifier in ATRT (Alimova et al., 2013; Kadoch et al., 2016; Moreno and Kerl, 2016). Despite the known interplay between Polycomb and SWI/SNF complexes (Kadoch et al., 2016), genetic targets of EZH2 in the context of SMARCB1-deficiency are very limited and restricted to rhabdoid cell lines (Wilson et al., 2010). To better understand the role of EZH2 in chromatin organization of ATRT, we generated genome-wide EZH2 ChIP-seq data for ATRTs across all three subgroups (Table S1). Identification of EZH2-occupied promoters revealed that eighty percent of all promoters bound by SMARCB1 in PNB and repressed in ATRT were indeed targeted by EZH2 (Figure 4A-4B). These data support the role of EZH2 in (a) establishing the transition from active to repressed chromatin states via deposition of H3K27me3 at SMARCB1 binding sites in ATRT and (b) being a rational therapeutic target. The other 20% of SMARCB1 bound promoters had no EZH2 binding in ATRT (Figure 4A), suggesting repressed chromatin organization at these loci without EZH2 involvement. Transcription factor motif enrichment analysis using known motifs (Figure 4C) and *de novo* identified motifs (data not shown) at SMARCB1-bound sites in promoters with repressive chromatin organization in ATRT pointed to the potential involvement of REST, a neuronal transcriptional repressor involved in chromatin organization (Arnold et al., 2013; Meier and Brehm, 2014). Interestingly, expression of REST was significantly higher in ATRT compared to PNB (Figure 4D). We performed REST ChIP-seq in seven primary ATRTs and identified REST to co-localize with EZH2 at SMARCB1 bound yet repressed genes in ATRT (Figure 4E). Plotting the REST occupancy surrounding  $\pm$  5kb TSS of such genes revealed REST localization often extending into gene body (Figure 4F), in line with EZH2 localization pattern at those loci (Figure 4G). Overall, these data suggest that in the absence of SMARCB1, EZH2 binding leads to gene silencing, probably in concert with other transcriptional repressors such as REST.

### ***Genes marked by EZH2 without H3K27me3 in ATRTs are expressed and are associated with active chromatin states***

Given the fact that we identified a large group of promoters which were SMARCB1 bound in PNB to be targeted by EZH2 in ATRT (Figure 4A), we thoroughly characterized EZH2 and H3K27me3 dynamics at all promoters in ATRT (Figure 5A). Surprisingly, we identified a large group of promoters bound by EZH2 but devoid of H3K27me3 (EZH2<sup>+</sup>/H3K27me3<sup>-</sup> promoters representing ~38% of all promoters, see also Figure S5A-S5B for the derivation of the applied cut-offs). EZH2<sup>+</sup>/H3K27me3<sup>-</sup> promoters were much more abundant than promoters with the expected co-occurrence of EZH2 and H3K27me3 (EZH2<sup>+</sup>/H3K27me3<sup>+</sup>, ~11% of all promoters). EZH2<sup>+</sup>/H3K27me3<sup>-</sup> promoters were present in all three ATRT subgroups (Figure S5C-S5E) and also very clearly present in BT16 ATRT cell line (Figure S5F) (no data for BT12) and in PNB (Figure S5G), but largely absent in ESC (Ku et al., 2008) (Figure S5H). ChIP-qPCR experiments confirmed the existence of a class of genes in ATRT that were occupied by EZH2 but had no H3K27me3 (Figure S5I-S5K). Existence of genes marked by EZH2 without H3K27me3 was previously shown for castration resistant prostate cancer cells (Xu et al., 2012). Here, we show that this is a prevalent class of genes in primary ATRTs and normal pediatric brain tissue as well.

Genes with EZH2<sup>+</sup>/H3K27me3<sup>-</sup> promoter status in ATRT were expressed at significantly higher levels (Figure 5B), showed promoter-hypomethylation (Figure 5C), and were associated with active chromatin states (Figure 5D), compared to genes associated with EZH2<sup>+</sup>/H3K27me3<sup>+</sup> promoters. The genes with promoters in EZH2<sup>+</sup>/H3K27me3<sup>-</sup> status and associated with EZH2 enrichments in the upper 5<sup>th</sup> percentile were significantly enriched for pathways regulating translation, cell cycle and chromatin organization (Table S3).

### ***Residual SWI/SNF activity maintains EZH2-occupied genes active***

It has been reported that loss of SMARCB1 causes disassembly of most SWI/SNF complexes at promoters and typical enhancers, but it is also known that there must be residual SWI/SNF activity in

the absence of SMARCB1 as rhabdoid cell lines have been shown to depend on SMARCA4 (Alver et al., 2017; Wang et al., 2017). To test whether residual SWI/SNF complex occupancy may be responsible for the active chromatin organization at EZH2<sup>+</sup>/H3K27me3<sup>-</sup> promoters, we generated SMARCA4 ChIP-seq data in different ATRTs across all three subgroups. Indeed, nearly all EZH2<sup>+</sup>/H3K27me3<sup>-</sup> promoters revealed SMARCA4 binding (Figure 6A, Figure S6) and 92.5% of them overlapped with SMARCB1 binding sites in PNB as well (Figure S7A). In contrast, EZH2<sup>+</sup>/H3K27me3<sup>+</sup> promoters showed almost no SMARCA4 binding (Figure 6B, Figure S6) and only 17.0% of such promoters showed both SMARCA4 occupancy in ATRT and SMARCB1 occupancy in PNB (Figure S7B). Additional ChIP-seq data generated for SUZ12, another component of the PRC2 complex (Grossniklaus and Paro, 2014), showed co-localization of SUZ12 with EZH2 at both EZH2<sup>+</sup>/H3K27me3<sup>-</sup> and EZH2<sup>+</sup>/H3K27me3<sup>+</sup> promoters (Figure 6A-6B, Figure S6). Interestingly, we also identified REST to anchor at TSS of EZH2<sup>+</sup>/H3K27me3<sup>-</sup> genes. However, as opposed to the localization at SMARCB1 bound yet repressed genes (~80% EZH2<sup>+</sup>/H3K27me3<sup>-</sup> status), REST binding at active loci was only focused at TSS without extension into the gene body (Figure S7C), consistent with previous publications (Rockowitz et al., 2014). Interestingly, in contrast to SMARCB1 bound yet repressed genes, we found no enrichment of the REST binding motif at these active loci, suggesting that REST is here not binding directly to the DNA. Altogether, these data suggests that residual SWI/SNF binding, as measured by SMARCA4 binding, ensures gene activity, and also enables oncogene activation such as *CDK4*, a prominent cell cycle gene deregulated in rhabdoid tumors (Moreno and Kerl, 2016), even in the presence of Polycomb complex (Figure 6C). Our findings, which demonstrate co-localization of SUZ12 together with EZH2 at EZH2<sup>+</sup>/H3K27me3<sup>-</sup> promoters (Figure 6A), make it unlikely that EZH2 specifically has a direct role on activation of EZH2<sup>+</sup>/H3K27me3<sup>-</sup> genes though an activating role for the whole PRC2 can not be directly excluded. To investigate this, we silenced EZH2 expression in BT16 cells using an inducible shRNA (Figure S7D) and analyzed gene expression profiles by RNA-seq. Differential gene expression analyses showed that 1151 genes were significantly  $\geq 2$ -fold upregulated after EZH2 knock-down, including 712 genes annotated as EZH2<sup>+</sup>/H3K27me3<sup>-</sup> genes and 110 genes

annotated as EZH2<sup>+</sup>/H3K27me3<sup>+</sup> genes (Figure S7E). ATRT ChIP-seq data for H3K27me3 showed that upregulated genes after EZH2 knock-down in BT16 cells display significantly higher H3K27me3 levels in primary ATRTs than downregulated genes, not only for EZH2<sup>+</sup>/H3K27me3<sup>+</sup> genes, but also for EZH2<sup>+</sup>/H3K27me3<sup>-</sup> genes where in general the H3K27me3 levels are much lower (Figure S7F, note that scales are different between left and right panel). These data suggest that upregulated genes after EZH2 knock-down are suppressed by EZH2 in ATRTs, not only for EZH2<sup>+</sup>/H3K27me3<sup>+</sup> genes, but also for EZH2<sup>+</sup>/H3K27me3<sup>-</sup> genes. However, suppression by EZH2 for the EZH2<sup>+</sup>/H3K27me3<sup>-</sup> genes is less strong, as reflected by the overall much lower levels of H3K27me3, due to the residual SWI/SNF complex present at these sites. Altogether, these data suggest that EZH2 still most likely acts as suppressor and not as an activator at EZH2<sup>+</sup>/H3K27me3<sup>-</sup> genes.

The existence of residual SWI/SNF activity in the absence of SMARCB1 has previously been implicated by showing that rhabdoid cell lines depend on SMARCA4 (Wang et al., 2009). While we found a significant reduction in representation of active enhancer state in ATRT (Figure 1B), we were interested in evaluating whether the residual SWI/SNF complex was present at enhancers that remained active in ATRT. We identified SMARCA4 localization at ATRT subgroup specific enhancers and the pattern of SMARCA4 occupancy in ATRT subgroups was concordant with the subgroup-specificity of the enhancers (Figure 6D). SMARCA4 binding at enhancers contained or not-contained within super-enhancers were largely comparable (Figure S7G). Further, co-localization of SMARCA4 and EZH2 was also found at active enhancers and super-enhancers, previously identified by genome-wide H3K27ac profiling (Johann et al., 2016) (Figure S7H-S7J).

As EZH2<sup>+</sup>/H3K27me3<sup>-</sup> class of promoters were also present in PNB (Figure S5G), we wondered about SWI/SNF and Polycomb interplay at such promoters in PNB. Interestingly, we identified a strong correlation between EZH2 and SMARCB1 occupancy and EZH2 and SMARCB1 co-localization at

EZH2<sup>+</sup>/H3K27me3<sup>-</sup> promoters in PNB (Figure S7K-S7L), indicating that the SWI/SNF and Polycomb co-localization does not specifically occur in ATRTs but also in normal tissue.

***SMARCA4 knock-down in ATRT cell lines results in growth arrest and reduction in the expression of genes occupied by EZH2 without H3K27me3.***

The binding of SMARCA4 at EZH2<sup>+</sup>/H3K27me3<sup>-</sup> promoters suggests that this SWI/SNF member may impede EZH2 function at these genes and thus maintains these genes in an active state. To validate this hypothesis, we performed SMARCA4 knock-downs in BT12 and BT16 ATRT cell lines using shRNAs (Figure S7M). SMARCA4 knock-down led to substantial reduction in growth rate in both ATRT cell lines caused by an increase in apoptosis (Figure 7A-7B). In comparison, SMARCA4 knock-down did not result in robust changes in growth rate of 293T cells, which has intact SMARCB1 (Figure 7A). SMARCA4 knockdown led to a downregulation of several key genes (Figure 7C), such as *CCND3* and *CDK6* related to cell death and survival and cell growth and proliferation, suggesting that SMARCA4 has an essential role in maintaining the proliferation and viability of rhabdoid cells. Furthermore, these genes have EZH2<sup>+</sup>/H3K27me3<sup>-</sup> promoter states in BT16 cell line, implying that reduction in the activity of SMARCA4 will result in an increase of H3K27me3 and loss of activity of the genes with EZH2<sup>+</sup>/H3K27me3<sup>-</sup> promoter status. Indeed, quantification of H3K27me3 levels by ChIP-qPCR after SMARCA4 knockdown showed a significant increase of H3K27me3 at these genes (Figure 7D).

## **DISCUSSION**

In this study, we present a full characterization of chromatin state dynamics in a primary tumor deficient for SMARCB1 by generating ChIP-seq data for six histone marks for 11 ATRTs representing all three molecular subgroups. Our data demonstrate a global loss of H3K27ac and H3K27me3 in the absence of SMARCB1 in ATRT (Figure 1). We identify genome-wide loss of H3K27ac-associated chromatin states in ATRT rather than a non-specific loss of all other active histone mark-associated states. Importantly, even though EZH2 expression is strongly upregulated in ATRT (Alimova et al.,

2013), this does not result in a global increase in H3K27me3 levels. In contrast, we observed a globally decreased H3K27me3 signal, in line with immunohistochemical observations (Hasselblatt et al., 2017; Kakkar et al., 2016; Venneti et al., 2014). As suggested previously, EZH2 overexpression might mainly be explained by the need to maintain H3K27me3 levels in proliferating cells (Wassef et al., 2015).

The epigenetic changes caused by SMARCB1 loss in ATRT were further validated in SMARCB1 re-expressing ATRT cell lines (n=2) by both ChIP-seq and gene expression profiling; in particular our findings re-emphasize the anti-proliferative functions of SMARCB1.

Although previous studies have highlighted the importance of EZH2 in rhabdoid tumors (Alimova et al., 2013; Kakkar et al., 2016; Kheradmand Kia et al., 2009; Knutson et al., 2013; Kurmasheva et al., 2017; Morel et al., 2017; Moreno and Kerl, 2016), its main targets in primary tumors so far remained ill-defined. Here, we re-define EZH2/Polycomb complex dynamics in ATRT. Our data show that residual SWI/SNF complex and Polycomb complex are co-localized at active genes in ATRTs where the residual SWI/SNF protects against Polycomb-mediated repression. At repressed genes - such as neuronal differentiation genes - the binding of residual SWI/SNF complex is most likely impeded by REST. These genes display an enrichment for REST signal, which probably directs the PRC2 complex to these genes, setting H3K27me3 marks. On the other hand, at enhancers and the majority of promoters, residual SWI/SNF localization ensures subgroup/lineage-specific enhancer activity, gene activity and possibly oncogene activation even in the presence of Polycomb (Figure 8). At these genetic regions we also did not detect any REST binding motif, and although REST signal is not completely absent in these regions, signals are much narrower than at repressed genes. This is also in accordance with previous data, showing narrow signals of REST at active genes (Rockowitz et al., 2014).

Hypothesizing that both the lineage determination as well as the oncogenic drive is dependent on residual SWI/SNF - EZH2 function in ATRT, design of therapies targeting residual SWI/SNF complex components alone or in combination with EZH2 inhibition might be beneficial for treatment of ATRT patients. However, therapies based on EZH2 inhibition alone may have the risk that not only repressed genes are re-activated but that active genes also become more active. As the malfunction/mutation of both SWI/SNF and Polycomb complexes is prevalent in many cancer types (Brien et al., 2016), and given the fact that we identified co-localization of SWI/SNF and Polycomb complexes at active genes both in ATRT and non-neoplastic tissue despite their known antagonistic functions (Kadoch et al., 2016), our findings will give directions both to the understanding of the basic biology between these complexes and discovery of novel regulatory mechanisms appearing as a result of their disruption.

## STAR METHODS

- **KEY RESOURCES TABLE**
- **CONTACT FOR REAGENT AND RESOURCE SHARING**
- **EXPERIMENTAL MODEL AND SUBJECT DETAILS**
- **METHOD DETAILS**
  - ChIP-sequencing
  - ChIP-qPCR
  - ModSpec Analysis of Histone Marks
  - Cell line cultures
  - Proliferation assay
  - Protein extraction and quantification
  - Protein electrophoresis and blotting
  - DNA/RNA extraction, purification, RNA quantification and quality assessment
  - Oligonucleotides
  - RT-qPCR
  - Lentiviral Production and Infection
  - Stable lentiviral infection of rhabdoid cells
  - Plasmids
  - Cell cycle analyses
  - Cell senescence analysis
  - EZH2 knock-down and RNA-seq
  - Genomic coordinates and gene annotation
  - Quantification of gene expression generated by RNA-seq
  - Chromatin segmentation



- **Multi-track representation of the data**
- **Comparison of chromatin state distributions**
- **DNA methylation analysis**
- **Regions losing and gaining H3K27ac/H3K27me3**
- **Representation of the genomic regions**
- **Peak finding**
- **SMARCB1 binding at different chromatin states**
- **Chromatin states of the promoters bound by SMARCB1**
- **Transcription factor motif finding**
- **Promoters according to EZH2 and H3K27me3 status**
- **Chromatin states at different EZH2/H3K27me3 classes**
- **Plotting ChIP-seq signal around TSS**
- **Pathway enrichment analysis**
- **QUANTIFICATION AND STATISTICAL ANALYSES**
- **DATA AND SOFTWARE AVAILABILITY**

## **SUPPLEMENTAL INFORMATION**

Supplemental Information includes eight supplementary figures, and three tables.

## **ACKNOWLEDGEMENTS**

We thank the DKFZ sequencing core facility and the Heidelberg Center for Personalized Oncology (DKFZ-HIPO) for technical support and funding through HIPO project H049, and Christina Jaeger-Schmidt, Jules Kerssemakers and Alke Jugold (German Cancer Research Center (DKFZ)) for technical assistance and data management. S.E is supported as a recipient of long term Human Frontiers Science Program (HFSP) postdoctoral fellowship (LT000432/2014). M.H is supported by DFG (HA 3060/5-1) and IZKF Münster (Ha3/019/15). CWMR is supported by NCI grants R01CA172152, R01CA113794 and P30CA021765. D.W. and M.A.F were funded as part of the INSTINCT network programme grant, co-funded by The Brain Tumour Charity, Great Ormond Street Children's Charity, and Children With Cancer UK (16/193). Additional support came from the ICGC DE-Mining grant (#01KU1505G). EZH2 knock-down RNA-seq analysis was performed by the St. Jude Children's Research Hospital Genome Sequencing Facility which is partially supported by the NCI Comprehensive Cancer Center Support Grant P30 CA021765.

## **AUTHOR CONTRIBUTIONS**

S.E., P.D.J. and M.A.F. contributed equally to the manuscript. S.M.P. and M.K. conceived the study. S.E., P.D.J., S.M.P., and M.K. wrote the manuscript with input from all co-authors. S.E., P.D.J., M.A.F., Y.D., H.C.C., D.S., D.T.W.J., S.W., J.P.M., K.B., P.A.N., J.O.K., P.L., R.E., C.W.M.R., and D.W. contributed to the design and conduct of experiments. S.E., P.D.J., H.C.C., M.Z., and L.C. performed bioinformatics analyses. A.K., M.R., and M.H. performed histopathological analyses of the samples. O.W., A.E.K., M.C.F., A.G., and M.H. provided tumor samples and metadata.

## **DECLARATION OF INTERESTS**

The authors declare no competing interests.

## **REFERENCES**

- Albanese, P., Belin, M. F., and Delattre, O. (2006). The tumour suppressor hSNF5/INI1 controls the differentiation potential of malignant rhabdoid cells. *Eur J Cancer* 42, 2326-2334.
- Alimova, I., Birks, D. K., Harris, P. S., Knipstein, J. A., Venkataraman, S., Marquez, V. E., Foreman, N. K., and Vibhakar, R. (2013). Inhibition of EZH2 suppresses self-renewal and induces radiation sensitivity in atypical rhabdoid teratoid tumor cells. *Neuro Oncol* 15, 149-160.
- Alver, B. H., Kim, K. H., Lu, P., Wang, X., Manchester, H. E., Wang, W., Haswell, J. R., Park, P. J., and Roberts, C. W. (2017). The SWI/SNF chromatin remodelling complex is required for maintenance of lineage specific enhancers. *Nat Commun* 8, 14648.
- Anders, S., Pyl, P. T., and Huber, W. (2015). HTSeq--a Python framework to work with high-throughput sequencing data. *Bioinformatics* 31, 166-169.

Arnold, P., Scholer, A., Pachkov, M., Balwierz, P. J., Jorgensen, H., Stadler, M. B., van Nimwegen, E., and Schubeler, D. (2013). Modeling of epigenome dynamics identifies transcription factors that mediate Polycomb targeting. *Genome Res* 23, 60-73.

Biswas, A., Kashyap, L., Kakkar, A., Sarkar, C., and Julka, P. K. (2016). Atypical teratoid/rhabdoid tumors: challenges and search for solutions. *Cancer Manag Res* 8, 115-125.

Brien, G. L., Valerio, D. G., and Armstrong, S. A. (2016). Exploiting the Epigenome to Control Cancer-Promoting Gene-Expression Programs. *Cancer Cell* 29, 464-476.

Chun, H. J., Lim, E. L., Heravi-Moussavi, A., Saberi, S., Mungall, K. L., Bilenky, M., Carles, A., Tse, K., Shlafman, I., Zhu, K., et al. (2016). Genome-Wide Profiles of Extra-cranial Malignant Rhabdoid Tumors Reveal Heterogeneity and Dysregulated Developmental Pathways. *Cancer Cell* 29, 394-406.

Dobin, A., Davis, C. A., Schlesinger, F., Drenkow, J., Zaleski, C., Jha, S., Batut, P., Chaisson, M., and Gingeras, T. R. (2013). STAR: ultrafast universal RNA-seq aligner. *Bioinformatics* 29, 15-21.

Encode Project Consortium (2012). An integrated encyclopedia of DNA elements in the human genome. *Nature* 489, 57-74.

Ernst, J., and Kellis, M. (2012). ChromHMM: automating chromatin-state discovery and characterization. *Nat Methods* 9, 215-216.

Fruhwald, M. C., Biegel, J. A., Bourdeaut, F., Roberts, C. W., and Chi, S. N. (2016). Atypical teratoid/rhabdoid tumors-current concepts, advances in biology, and potential future therapies. *Neuro Oncol* 18, 764-778.

Garcia, B. A., Mollah, S., Ueberheide, B. M., Busby, S. A., Muratore, T. L., Shabanowitz, J., and Hunt, D. F. (2007). Chemical derivatization of histones for facilitated analysis by mass spectrometry. *Nat Protoc* 2, 933-938.

Ginn, K. F., and Gajjar, A. (2012). Atypical teratoid rhabdoid tumor: current therapy and future directions. *Front Oncol* 2, 114.

Grossniklaus, U., and Paro, R. (2014). Transcriptional silencing by polycomb-group proteins. *Cold Spring Harb Perspect Biol* 6, a019331.

Hasselblatt, M., Johann, P. D., Kool, M., and Fruhwald, M. C. (2017). Reduced histone H3 K27 trimethylation is encountered in about 50% of atypical teratoid/rhabdoid tumors (AT/RT) but is not associated with molecular subgroup status and outcome. *Acta Neuropathol* 134, 817-818.

Hasselblatt, M., Nagel, I., Oyen, F., Bartelheim, K., Russell, R. B., Schuller, U., Junckerstorff, R., Rosenblum, M., Alassiri, A. H., Rossi, S., et al. (2014). SMARCA4-mutated atypical teratoid/rhabdoid tumors are associated with inherited germline alterations and poor prognosis. *Acta Neuropathol* 128, 453-456.

Johann, P. D., Erkek, S., Zapatka, M., Kerl, K., Buchhalter, I., Hovestadt, V., Jones, D. T., Sturm, D., Hermann, C., Segura Wang, M., et al. (2016). Atypical Teratoid/Rhabdoid Tumors Are Comprised of Three Epigenetic Subgroups with Distinct Enhancer Landscapes. *Cancer Cell* 29, 379-393.

Kadoch, C., Copeland, R. A., and Keilhack, H. (2016). PRC2 and SWI/SNF Chromatin Remodeling Complexes in Health and Disease. *Biochemistry* 55, 1600-1614.

Kadoch, C., Hargreaves, D. C., Hodges, C., Elias, L., Ho, L., Ranish, J., and Crabtree, G. R. (2013). Proteomic and bioinformatic analysis of mammalian SWI/SNF complexes identifies extensive roles in human malignancy. *Nat Genet* 45, 592-601.

Kakkar, A., Biswas, A., Goyal, N., Suri, V., Sharma, M. C., Gupta, D., Julka, P. K., and Sarkar, C. (2016). The Expression of Cyclin D1, VEGF, EZH2, and H3K27me3 in Atypical Teratoid/Rhabdoid Tumors of the CNS: A Possible Role in Targeted Therapy. *Appl Immunohistochem Mol Morphol* 24, 729-737.

Kheradmand Kia, S., Solaimani Kartalaei, P., Farahbakhshian, E., Pourfarzad, F., von Lindern, M., and Verrijzer, C. P. (2009). EZH2-dependent chromatin looping controls INK4a and INK4b, but not ARF, during human progenitor cell differentiation and cellular senescence. *Epigenetics Chromatin* 2, 16.

Kim, K. H., Kim, W., Howard, T. P., Vazquez, F., Tsherniak, A., Wu, J. N., Wang, W., Haswell, J. R., Walensky, L. D., Hahn, W. C., et al. (2015). SWI/SNF-mutant cancers depend on catalytic and non-catalytic activity of EZH2. *Nat Med* 21, 1491-1496.

Kim, K. H., and Roberts, C. W. (2014). Mechanisms by which SMARCB1 loss drives rhabdoid tumor growth. *Cancer Genet* 207, 365-372.

Knutson, S. K., Warholic, N. M., Wigle, T. J., Klaus, C. R., Allain, C. J., Raimondi, A., Porter Scott, M., Chesworth, R., Moyer, M. P., Copeland, R. A., et al. (2013). Durable tumor regression in genetically altered malignant rhabdoid tumors by inhibition of methyltransferase EZH2. *Proc Natl Acad Sci U S A* 110, 7922-7927.

Ku, M., Koche, R. P., Rheinbay, E., Mendenhall, E. M., Endoh, M., Mikkelsen, T. S., Presser, A., Nusbaum, C., Xie, X., Chi, A. S., et al. (2008). Genomewide analysis of PRC1 and PRC2 occupancy identifies two classes of bivalent domains. *PLoS Genet* 4, e1000242.

Kurmasheva, R. T., Sammons, M., Favours, E., Wu, J., Kurmashev, D., Cosmopoulos, K., Keilhack, H., Klaus, C. R., Houghton, P. J., and Smith, M. A. (2017). Initial testing (stage 1) of tazemetostat (EPZ-6438), a novel EZH2 inhibitor, by the Pediatric Preclinical Testing Program. *Pediatr Blood Cancer* 64.

Law, C. W., Chen, Y., Shi, W., and Smyth, G. K. (2014). voom: Precision weights unlock linear model analysis tools for RNA-seq read counts. *Genome Biol* 15, R29.

Lin, C. Y., Erkek, S., Tong, Y., Yin, L., Federation, A. J., Zapatka, M., Haldipur, P., Kawauchi, D., Risch, T., Warnatz, H. J., et al. (2016). Active medulloblastoma enhancers reveal subgroup-specific cellular origins. *Nature* 530, 57-62.

MacLean, B., Tomazela, D. M., Shulman, N., Chambers, M., Finney, G. L., Frewen, B., Kern, R., Tabb, D. L., Liebler, D. C., and MacCoss, M. J. (2010). Skyline: an open source document editor for creating and analyzing targeted proteomics experiments. *Bioinformatics* 26, 966-968.

Masliyah-Planchon, J., Bieche, I., Guinebretiere, J. M., Bourdeaut, F., and Delattre, O. (2015). SWI/SNF chromatin remodeling and human malignancies. *Annu Rev Pathol* 10, 145-171.

Meerbrey, K. L., Hu, G., Kessler, J. D., Roarty, K., Li, M. Z., Fang, J. E., Herschkowitz, J. I., Burrows, A. E., Ciccia, A., Sun, T., et al. (2011). The pINDUCER lentiviral toolkit for inducible RNA interference in vitro and in vivo. *Proc Natl Acad Sci U S A* 108, 3665-3670.

Meier, K., and Brehm, A. (2014). Chromatin regulation: how complex does it get? *Epigenetics* 9, 1485-1495.

Morel, D., Almouzni, G., Soria, J. C., and Postel-Vinay, S. (2017). Targeting chromatin defects in selected solid tumors based on oncogene addiction, synthetic lethality and epigenetic antagonism. *Ann Oncol* 28, 254-269.

Moreno, N., and Kerl, K. (2016). Preclinical Evaluation of Combined Targeted Approaches in Malignant Rhabdoid Tumors. *Anticancer Res* 36, 3883-3887.

Pfister, S. M., Korshunov, A., Kool, M., Hasselblatt, M., Eberhart, C., and Taylor, M. D. (2010). Molecular diagnostics of CNS embryonal tumors. *Acta Neuropathol* 120, 553-566.

Roadmap Epigenomics Consortium, Kundaje, A., Meuleman, W., Ernst, J., Bilenky, M., Yen, A., Heravi-Moussavi, A., Kheradpour, P., Zhang, Z., Wang, J., et al. (2015). Integrative analysis of 111 reference human epigenomes. *Nature* 518, 317-330.

Robinson, M. D., and Oshlack, A. (2010). A scaling normalization method for differential expression analysis of RNA-seq data. *Genome Biol* 11, R25.

Rockowitz, S., Lien, W. H., Pedrosa, E., Wei, G., Lin, M., Zhao, K., Lachman, H. M., Fuchs, E., and Zheng, D. (2014). Comparison of REST cistromes across human cell types reveals common and context-specific functions. *PLoS Comput Biol* 10, e1003671.

Sarbassov, D. D., Guertin, D. A., Ali, S. M., and Sabatini, D. M. (2005). Phosphorylation and regulation of Akt/PKB by the rictor-mTOR complex. *Science* 307, 1098-1101.

Schneppenheim, R., Fruhwald, M. C., Gesk, S., Hasselblatt, M., Jeibmann, A., Kordes, U., Kreuz, M., Leuschner, I., Martin Subero, J. I., Obser, T., et al. (2010). Germline nonsense mutation and somatic inactivation of SMARCA4/BRG1 in a family with rhabdoid tumor predisposition syndrome. *Am J Hum Genet* 86, 279-284.

Stunnenberg, H. G., International Human Epigenome, C., and Hirst, M. (2016). The International Human Epigenome Consortium: A Blueprint for Scientific Collaboration and Discovery. *Cell* 167, 1145-1149.

Torchia, J., Golbourn, B., Feng, S., Ho, K. C., Sin-Chan, P., Vasiljevic, A., Norman, J. D., Guilhamon, P., Garzia, L., Agamez, N. R., et al. (2016). Integrated (epi)-Genomic Analyses Identify Subgroup-Specific Therapeutic Targets in CNS Rhabdoid Tumors. *Cancer Cell* 30, 891-908.

Venneti, S., Santi, M., Felicella, M. M., Yarin, D., Phillips, J. J., Sullivan, L. M., Martinez, D., Perry, A., Lewis, P. W., Thompson, C. B., and Judkins, A. R. (2014). A sensitive and specific histopathologic prognostic marker for H3F3A K27M mutant pediatric glioblastomas. *Acta Neuropathol* 128, 743-753.

Wang, X., Lee, R. S., Alver, B. H., Haswell, J. R., Wang, S., Mieczkowski, J., Drier, Y., Gillespie, S. M., Archer, T. C., Wu, J. N., et al. (2017). SMARCB1-mediated SWI/SNF complex function is essential for enhancer regulation. *Nat Genet* 49, 289-295.

Wang, X., Sansam, C. G., Thom, C. S., Metzger, D., Evans, J. A., Nguyen, P. T., and Roberts, C. W. (2009). Oncogenesis caused by loss of the SNF5 tumor suppressor is dependent on activity of BRG1, the ATPase of the SWI/SNF chromatin remodeling complex. *Cancer Res* 69, 8094-8101.



Wassef, M., Rodilla, V., Teissandier, A., Zeitouni, B., Gruel, N., Sadacca, B., Irondelle, M., Charruel, M., Ducos, B., Michaud, A., et al. (2015). Impaired PRC2 activity promotes transcriptional instability and favors breast tumorigenesis. *Genes Dev* 29, 2547-2562.

Wilson, B. G., Wang, X., Shen, X., McKenna, E. S., Lemieux, M. E., Cho, Y. J., Koellhoffer, E. C., Pomeroy, S. L., Orkin, S. H., and Roberts, C. W. (2010). Epigenetic antagonism between polycomb and SWI/SNF complexes during oncogenic transformation. *Cancer Cell* 18, 316-328.

Xu, K., Wu, Z. J., Groner, A. C., He, H. H., Cai, C., Lis, R. T., Wu, X., Stack, E. C., Loda, M., Liu, T., et al. (2012). EZH2 oncogenic activity in castration-resistant prostate cancer cells is Polycomb-independent. *Science* 338, 1465-1469.

Zhao, M., Sun, J., and Zhao, Z. (2013). TSGene: a web resource for tumor suppressor genes. *Nucleic Acids Res* 41, D970-976.

## FIGURE LEGENDS

### **Figure 1. The chromatin segmentation landscape of ATRT.**

**(A)** Roadmap 18-state chromatin segmentation model and the analyzed histone modifications.

**(B-G)** Comparison of the representation of selected chromatin states in ATRT (n=11) to the ones in GBM (n=3), MB (n=23), adult normal brain (Roadmap Epigenomics Consortium et al., 2015) (ANB) (n=7), pediatric normal brain (PNB) (n=1), and ESC (Roadmap Epigenomics Consortium et al., 2015) (n=5). Boxplots show the coverage of the selected chromatin states in the genome that show significant variability in ATRTs when compared to other tissues (EnhA1 (B), Tx (C), TssA (D), TssFlnkD (E), ReprPC (F), and Quies (G)) in the genome. \*Pair-wise t-test, adjusted p value < 0.05.

**(H)** Snapshots show the overlayed histone modification profiles and chromatin segmentation produced using the Roadmap 18-state model for selected ATRT signature genes for 11 ATRTs representing ATRT-TYR (n=5), ATRT-SHH (n=3) and ATRT-MYC (n=3) subgroups at *CCND1* locus, *FOXK1* locus and *HOXC* cluster.

See also Figure S1 and S2 and Table S1.

**Figure 2. Re-expression of SMARCB1 in BT16 and BT12 ATRT cell lines results in global gain of H3K27ac.**

**(A)** Cartoon illustrating the experiments carried out in BT12 and BT16 ATRT cell lines after re-expression of *SMARCB1*.

**(B-C)** MA (M, log-ratio, A, mean average) plot-comparisons of average H3K27ac levels and log2 fold changes after *SMARCB1* re-expression indicate a substantially higher number of 2kb windows tiling the genome that gained H3K27ac compared to the ones that lose H3K27ac. Experiments were done for BT12 (B) and BT16 (C). Red dashed lines indicate the log2 fold changes at 0.5 and -0.5.

**(D-E)** Pie-charts display the genomic representation of the regions gaining or losing H3K27ac after *SMARCB1* re-expression in BT12 (D) and BT16 (E).

**(F)** Venn-diagram showing the overlap of the genomic regions gaining H3K27ac after *SMARCB1* re-expression in BT12 and BT16 cell lines.

**(G)** Snapshot displays H3K27ac (orange) and H3K27me3 (gray) signal at the genomic region chr22:30,578,739-30,634,209 before and after *SMARCB1* re-expression in BT12 cell line (top panel) and BT16 cell line (bottom panel).

**(H)** Scatter plot shows the correlation between average log2 fold change in expression and average log2 fold change in H3K27ac after re-expression of *SMARCB1* in BT12 and BT16 cell lines.

See also Figure S3.

**Figure 3. SMARCB1 binding sites: Repression of SMARCB1-bound genes via gain of H3K27me3 in ATRT.**

**(A)** Representation of SMARCB1 binding sites at different chromatin states in ATRT and pediatric normal brain (indicated as “normal” on the plot) highlights the association of SMARCB1 binding sites preferentially with repressed chromatin states in ATRT. Observed/expected state frequencies at SMARCB1 binding sites refer to the calculated odd ratios upon comparing the chromatin state representations at SMARCB1 binding sites with the genomic regions with similar genomic characteristics as SMARCB1 binding sites. See methods for details. H3K27ac-dominated and H3K27me3-dominated chromatin states are indicated with red and gray stars, respectively.

**(B)** Heatmaps displaying scaled-read densities for H3K27ac and H3K27me3 surrounding  $\pm 2$  kb TSS of the genes which are SMARCB1 bound in pediatric normal brain (normal) and comprise repressed chromatin states in ATRT (n=1791 unique promoters corresponding to n=689 unique genes).

**(C)** Association of SMARCB1 bound yet repressed promoters with neuronal differentiation genes in ATRT. Left panel shows the pathway enrichment analysis for the same set of genes as in (B). Snapshot (right panel) displays the SMARCB1 signal and the active chromatin states in pediatric normal brain (n=1), and repressed chromatin states in ATRT subgroups (TYR, n=5, SHH, n=3, MYC, n=3) at *NEUROD2* locus. The expression level of *NEUROD2* in ATRT subgroups in comparison to pediatric normal brain is presented as boxplot right to the image.

See also Figure S4 and Table S2.

**Figure 4. SMARCB1 bound genes in pediatric normal brain are mainly repressed via EZH2 in ATRT.**

**(A)** Barplot depicts the high fraction of promoters bound by SMARCB1 in pediatric normal brain but repressed in ATRT (Figure 3B) that are bound by EZH2 (80%), which illustrates the role of EZH2 in gain of H3K27me3 at SMARCB1 binding sites in ATRT. See methods for the definition of EZH2-bound promoters.

**(B)** Snapshots display the PNB SMARCB1 and multilayer-overlay EZH2 ChIP-seq signal in ATRT subgroups, and the chromatin segmentations at *EPHB1* (upper panel) and *CNR1* (lower panel) in PNB (n=1) and ATRT subgroups (TYR, n=5, SHH, n=3, and MYC, n=3). Boxplots next to the snapshots show the expression of the respective genes in ATRT subgroups and PNB.

**(C)** Top three known enriched transcription factor motifs identified by Homer.

**(D)** Boxplot showing the expression of *REST* in ATRT and PNB. \* Wilcoxon test p value = 0.01.

**(E)** The scatter plots shows the co-localization of REST and EZH2 at SMARCB1 bound repressed genes in ATRT.

**(F-G)** Heatmaps displaying the scaled-read density for REST (F) and EZH2 (G) at regions surrounding  $\pm$  5 kb TSS of the genes bound by SMARCB1 yet repressed in ATRT. At the top, density plot shows the average signal intensity displayed in the heatmap below.

**Figure 5. Delineation of a class of genes bound by EZH2 without H3K27me3 occupancy.**

**(A)** Scatter plot shows the comparison of the average EZH2 and H3K27me3 signal in ATRTs at promoter regions ( $\pm$  1kb Tss) of protein-coding genes (n=73104). Dashed red lines depict the cut-offs used to define EZH2<sup>+</sup> or H3K27me3<sup>+</sup> promoters (See methods). Fractions of promoters with EZH2<sup>+</sup>/H3K27me3<sup>-</sup> and EZH2<sup>+</sup>/H3K27me3<sup>+</sup> states are indicated as (1) and (2) on the plot, respectively.

**(B-C)** Boxplots display the expression (B) and DNA methylation (C) levels of the genes associated with different H3K27me3/EZH2 promoter classes in ATRT as indicated in (A). \*Wilcoxon test p value < 2.2e-16.

**(D)** Heatmaps depict the association of EZH2<sup>+</sup>/H3K27me3<sup>-</sup> promoters (n= 27483, EZH2<sup>+</sup>/H3K27me3<sup>-</sup> status in all ATRT subgroups) with active chromatin states and the preferential marking of EZH2<sup>+</sup>/H3K27me3<sup>+</sup> promoters (n=7829, EZH2<sup>+</sup>/H3K27me3<sup>+</sup> status in all ATRT subgroups) by repressed chromatin states, respectively at 200 bp windows surrounding  $\pm$  5kb TSS in ATRT. For visualization purposes, 1000 genes were randomly chosen from each category.

See also Figure S5 and Table S3.

**Figure 6. Residual SWI/SNF occupancy maintains gene and enhancer activity in ATRT.**

**(A-B)** Heatmaps displaying the scaled-read densities for EZH2 (blue), SUZ12 (brown), SMARCA4 (red) and H3K27me3 (dark gray) at regions surrounding  $\pm 2$  kb TSS of the genes highlight the co-localization of EZH2, SUZ12 and SMARCA4 at EZH2<sup>+</sup>/H3K27me3<sup>-</sup> promoters (A) and the lack of SMARCA4 signal at EZH2<sup>+</sup>/H3K27me3<sup>+</sup> promoters (B) in ATRT, respectively. At the top, density plots show the average signal intensities displayed in the heatmaps below. For visualization purposes, 2000 randomly chosen promoters are shown either from EZH2<sup>+</sup>/H3K27me3<sup>-</sup> or EZH2<sup>+</sup>/H3K27me3<sup>+</sup> classes.

**(C)** Snapshot displaying the subgroup-multilayer EZH2, SUZ12 and SMARCA4 and H3K27me3 signals in ATRT-TYR (upper panel), ATRT-SHH (middle panel) and ATRT-MYC (lower panel) at *CDK4* locus.

**(D)** Heatmaps show the scaled average SMARCA4 signal in TYR, SHH and MYC subgroups at TYR-specific enhancers (top panels), SHH-specific enhancers (middle panels) and MYC-specific enhancers (bottom panels), respectively. EMP refers to the enhancer coordinate midpoints.

See also Figure S6 and Figure S7.

**Figure 7. SMARCA4 knock-down in ATRT cell lines.**

**(A)** Growth curves assay of SMARCA4 knockdown in BT12, BT16 and 293T cells. Each data point represents the average of two independent experiments. The data results of the growth curve were converted to a percentage, as the cells had different growth rate. The results were analyzed based on two way variance analysis (ANOVA). The analysis was performed using GraphPad Prism 6.0 software (Version 7.00, GraphPad Software, San Diego, CA, USA, 2017).  $p \leq 0.01$  (\*);  $p \leq 0.001$  (\*\*),  $p \leq 0.001$  (\*\*\*) and  $p \leq 0.0001$  (\*\*\*\*).

**(B)** Cell cycle analysis after SMARCA4 knock-down in BT12 and BT16. \* 2 way anova p value < 0.05.

**(C)** qRT-PCR measuring expression of cell cycle genes (*CDKN2A* (*p16*), *CDKN1A* (*p21*), *CCND3*, *CDK2* and *CDK6*) in BT12 and BT16 cell lines at 5 days following SMARCA4 knock down calibrated to expression of the empty vector ; mean of triplicates, error bars represents standard deviation.

**(D)** Plots show the normalized H3K27me3 quantifications at *CDKN2A*, *CDKN1A*, *CCND3*, and *CDK2*, *CDK6* promoters. Columns, mean of biological duplicates; bars, SD. \*adjP < 0.05 , \*\*adjP <0.005, \*\*\*adjP <0.0005, and \*\*\*\*adjP <0.0001, relative to the Plko.1 control (two way Anova test).

**Figure 8. Model summarizing the Polycomb - SWI/SNF interplay in the regulation of enhancer and gene activity in ATRTs.**

## STAR METHODS

(see also Figure S8)

## KEY RESOURCES TABLE

REAGENT or RESOURCE	SOURCE	IDENTIFIER
Antibodies		
H3K27me3	Millipore Diagenode Cell Signaling Technologies	Cat#07-449 Cat#C15410195 Cat#9733
H3K4me1	ActiveMotif	Cat#39298
H3K4me3	ActiveMotif Diagenode	Cat#39159 Cat# C15410003-50
H3K9me3	ActiveMotif	Cat#39161
H3K36me3	ActiveMotif	Cat#61101
EZH2	ActiveMotif Cell Signaling Technologies	Cat#39901 Cat#5246
SMARCB1	Abcam	Cat#12167
SUZ12	ActiveMotif	Cat#39357
SMARCA4	Abcam Santacruz	Cat#110641 Cat# sc-17796
REST	Millipore	Cat#17-641
BAF47	BD Bioscience	Cat#612110
H3	Abcam Diagenode Cell Signaling Technologies	Cat#1791 Cat# C15210011 Cat#9715
B-actin	Abcam	Cat#49900
Anti-Mouse IgG	Abcam	Cat#6728
Anti-Rabbit IgG	Abcam	Cat#205718
Bacterial and Virus Strains		
<i>E.coli</i> DH5α	Invitrogen	Cat#18265017
Chemicals, Peptides, and Recombinant Proteins		
Trypan blue	Invitrogen	Cat# T10282
RNase	Sigma-Aldrich	Cat# R6148

Propidium iodide	Sigma-Aldrich	Cat# P4864
SDS-PAGE loading buffer	ThermoScientific	Cat# 11809340
4-20% polyacrylamide Amersham ECL Gel	GE Healthcare	Cat#45-002-470
SDS-PAGE Protein Ladder	ThermoScientific	Cat# 11842124
PVDF Transfer Membrane	ThermoScientific	Cat# 88518
Puromycin	Gibco	Cat# A1113803
DMEM	Sigma	Cat# D5546
L-glutamine	Sigma	Cat# G7513
Pen-strep	Sigma	Cat# P4333
Fetal bovine serum	Gibco	Cat# 10082147
Trizol	ThermoFisher Scientific	Cat# 15596026
Tet-Free FBS	Clontech	Cat# 631106
<b>Critical Commercial Assays</b>		
CellTiter-Glo® Luminescent Cell Viability Assay	Promega	Cat# G7570
Subcellular Protein Fractionation Kit	Pierce	Cat# 78840
BCA Protein Assay Kit	Pierce	Cat# 23225
SuperSignal West Pico Chemiluminescent Substrate	Pierce	Cat#34577
DNA/RNA Miniprep Kit	Zymo	Cat#D7001
RNA 6000 Nano Kit	Agilent	Cat# 5067-1512
High-Capacity RNA-to-cDNA Kit	Applied Biosystems	Cat#4387406
Platinum SYBR Green qPCR Supermix – UDG with ROX kit	Invitrogen	Cat# 11744500
CalPhos™ Mammalian Transfection Kit	Clontech	Cat# 631312
Senescence detection kit	Sigma Aldrich	Cat# CS0030-1KT
DirectZol Mini Prep Plus Kit	Zymo research	Cat# R2070
<b>Deposited Data</b>		
Raw data	This paper	EGAS00001001297 with dataset group number EGAD00001003408
<b>Experimental Models: Cell Lines</b>		
Human: 293T	ATCC	Cat#CRL-3216
Human: BT12	COG cells	N/A
Human: BT16	COG cells	N/A
<b>Oligonucleotides</b>		
GAPDH (RT-qPCR) F CAGGTCATCCATGACAACTTTG	Sigma Aldrich	N/A
GAPDH (RT-qPCR) R GTCCACCACCCTGTTGCTGTAG	Sigma Aldrich	N/A
CDKN2A (RT-qPCR) F CCCTCAGACATCCCCGATT	Sigma Aldrich	N/A
CDKN2A (RT-qPCR) R TCTAAGTTTCCCGAGGTTTCTCA	Sigma Aldrich	N/A
CDKN1A (RT-qPCR) F GGCAGACCAGCATGACAGATT	Sigma Aldrich	N/A
CDKN1A (RT-qPCR) R GCGGATTAGGGCTTCCTCT	Sigma Aldrich	N/A
CCND1 (RT-qPCR) F GCCGTCCATGCGGAAGATC	Sigma Aldrich	N/A
CCND1 (RT-qPCR) R CCTCCTCCTCGCACTTCTGT	Sigma Aldrich	N/A
CCND3 (RT-qPCR) F CAGGCCTTGGTCAAAAAGCA	Sigma Aldrich	N/A
CCND3 (RT-qPCR) R GCGGGTACATGGCAAAGGTA	Sigma Aldrich	N/A
CDK6 (RT-qPCR) F CTTGAGCACCCCAACGT	Sigma Aldrich	N/A

CDK6 (RT-qPCR) R GGTTCCTCTGTCTGTTCTGACACT	Sigma Aldrich	N/A
CDK2 (RT-qPCR) F CCAGGAGTTACTTCTATGCCTGA	Sigma Aldrich	N/A
CDK2 (RT-qPCR) R TTCATCCAGGGGAGGTACAAC	Sigma Aldrich	N/A
CDK2 (ChIP-qPCR) F CGTTCATCTCTTCCTCCTCT	Sigma Aldrich	N/A
CDK2 (ChIP-qPCR) R GAGATTAGGAAAAGGGGTCTGA	Sigma Aldrich	N/A
CDK6 (ChIP-qPCR) F GTGGTAGAAAGAATGTGTTT	Sigma Aldrich	N/A
CDK6 (ChIP-qPCR) R GGACTCTAGTCACCCAGGAA	Sigma Aldrich	N/A
CCND3 (ChIP-qPCR) F CGCATTCCTTAGAGCAAGCA	Sigma Aldrich	N/A
CCND3 (ChIP-qPCR) R GGACTCTAGTCACCCAGGAA	Sigma Aldrich	N/A
CDKN1A (ChIP-qPCR) F TATATCAGGGCCGCGCTG	Sigma Aldrich	N/A
CDKN1A (ChIP-qPCR) R GGCTCCACAAGGAAGTACTTC	Sigma Aldrich	N/A
CDKN2A (ChIP-qPCR) F CCCGTCCGTATTAAATAAACC	Sigma Aldrich	N/A
CDKN2A (ChIP-qPCR) R GGGTGTTTGGTGTCATAGGG	Sigma Aldrich	N/A
Recombinant DNA		
psPAX2	Addgene	Cat# 12260
pCDH-CMV-MCS-EF1-Puro	System BioScience	Cat# CD511B-1
pMD2.G	Addgene	Cat# 12259
Mission shRNA BRG1	Sigma Aldrich	N/A
pLKO.1-puro	Sigma Aldrich	Cat# SHC001
Software and Algorithms		
FlowJo	Stadnisky and Quinn. 2014	<a href="https://www.flowjo.com/">https://www.flowjo.com/</a>
quasR	Gaidatzis et al., 2015	<a href="https://bioconductor.org/packages/release/bioc/html/QuasR.html">https://bioconductor.org/packages/release/bioc/html/QuasR.html</a>
chromHMM	Ernst and Kellis, 2012	<a href="http://compbio.mit.edu/ChromHMM/">http://compbio.mit.edu/ChromHMM/</a>
Bedtools	Quinlan and Hall, 2010	<a href="http://bedtools.readthedocs.io/en/latest/">http://bedtools.readthedocs.io/en/latest/</a>
DeepTools	Ramirez et al., 2014	<a href="https://deeptools.readthedocs.io/en/develop/">https://deeptools.readthedocs.io/en/develop/</a>
MACS	Zhang et al., 2008	<a href="http://liulab.dfci.harvard.edu/MACS/">http://liulab.dfci.harvard.edu/MACS/</a>
HOMER	Heinz et al., 2010	<a href="http://homer.ucsd.edu/homer/">http://homer.ucsd.edu/homer/</a>
Mclust	N/A	<a href="http://www.stat.washington.edu/mclust">http://www.stat.washington.edu/mclust</a>
R functions for analysis of next generation sequencing data	Hisano et al., 2013	<a href="https://www.nature.com/articles/nprot.2013.145#supplementary-information">https://www.nature.com/articles/nprot.2013.145#supplementary-information</a>
ClueGO	Bindea et al., 2009	<a href="http://apps.cytoscape.org/apps/cluego">http://apps.cytoscape.org/apps/cluego</a>



## CONTACT FOR REAGENT AND RESOURCE SHARING

Further information and requests for resources should be directed to and will be fulfilled by the Lead Contact, Marcel Kool (m.kool@kitz-heidelberg.de).

## EXPERIMENTAL MODEL AND SUBJECT DETAILS

This study involves no new patient sample collection and informed consent exists for all patients contributing to the study. Patient samples, FF or formalin-fixed paraffin-embedded (FFPE) tumor samples, and peripheral blood samples, were obtained from the EU-RHAB registry and the following single institutions: University Hospital Heidelberg, NN Burdenko Neurosurgical Institute, University of Muenster, McGill University, University of Barcelona, University of Prague, St. Judes Children's Research Hospital, University of Bonn, University of Zuerich. All tumors were banked at the time of primary diagnosis between 2009 and 2015 in accordance with research ethics board approval from the respective institutes. Informed consent was obtained from all subjects included in the study.

All samples were histologically verified ATRTs (as diagnosed by local pathologists using INI1 and SMARCA4 immunohistochemistry). DNA and RNA were isolated from the FF tumor samples, and only DNA was isolated from the FFPE tumor and blood samples using standard procedures. In a subset of tumor samples, the type of *SMARCB1* mutation was characterized using MLPA, Sanger sequencing, or FISH as described above (Jackson et al., 2009). Molecular subgrouping was performed using either the 450k methylation or Affymetrix gene expression data (for subgroup information see Table S1).

## METHOD DETAILS

### ChIP-sequencing

ChIP experiments and library preparation for H3K27me3, H3K4me1, H3K4me3, H3K9me3, H3K36me3, EZH2, SMARCB1, SUZ12, SMARCA4 and REST ChIP was performed at ActiveMotif (Carlsbad, CA) using antibodies against H3K27me3 (#07-449, Millipore), H3K4me1 (AM#39298, ActiveMotif), H3K4me3 (AM#39159, ActiveMotif), H3K9me3 (AM#39161, ActiveMotif) and H3K36me3 (AM#61101, ActiveMotif), EZH2 (AM#39901, ActiveMotif), SMARCB1 (ab12167, Abcam), SUZ12 (AM#39357, ActiveMotif), SMARCA4 (ab110641, Abcam) and REST (ab17-641, Millipore). Resulting libraries were sequenced on the Illumina HiSeq 2000 platform (single-end, read length: 50 bp) according to the manufacturer's instructions. Alignment, and downstream processing of ChIP-seq data was performed as described (Johann et al., 2016). Full list of the ChIP-seq libraries generated can be found in Table S1. H3K27ac ChIP-seq data was already available from (Johann et al., 2016). Example ChIP-qPCR data for the six histone modifications and number of aligned reads obtained for the respective histone modification ChIP-seqs are presented in Figure S8.

### ChIP-qPCR

Cells were detached using 1% trypsin and washed twice with PBS. Cells were fixed with formaldehyde (1% final concentration; 28906, Pierce) for 8 min at RT, followed by 5 min incubation at RT with Glycine (50046, 125 mM final concentration). Cells were washed twice with cold PBS and lysed by douncing with 20 gauge needle x 20 times in cold Farnham buffer (47 mM, PIPES- P8203 Sigma, 3 M KCl- P9333 Sigma, 5% NP-40- I8896 Sigma; Proteinase inhibitors- 37491 Active motif); nuclei were resuspended in RIPA buffer (5% NP40, 5% Na deoxycholate- D6750 Sigma, 10% SDS, Proteinase inhibitors) and sonicated (Bioruptor; Diagenode) at high setting 30 seconds ON, 30 seconds OFF.

Immunoprecipitation was conducted with antibody specific to H3K27me3 (c15410069 Diagenode), H3 (ab12079 Abcam), and normal Rabbit IgG (ab171870, Abcam) coupled with M-280 Sheep Anti-Rabbit (11204D, Thermofisher). Samples were incubated with to the beads slurry for 2 h, after the antibodies were coupled with the beads for 2h at 4°C and washed with PBS/BSA (1xPBS, 5mg/ml BSA-15260037 Thermofisher). The beads were washed LiCl Wash Buffer at RT (100 mM Tris pH 7.5-10812846001 Roche / 500 mM LiCl / 1% NP-40 / 1% sodium deoxycholate) and TE (10 mM Tris-HCl pH 7.5 / 0.1 mM EDTA-EDS Sigma) before being resuspended in Elution Buffer (1% SDS- L6026 Sigma / 0.1 M NaHCO<sub>3</sub>- S5761 Sigma).

DNA were reverse cross-linked by incubation at 65 °C overnight, purified using ChIP DNA Clean & Concentrator Kit (D5205, Zymo research) and a fraction was used as template in real-time PCR reactions. DNA present in each immunoprecipitation was quantified by realtime qRT-PCR using gene-specific primers on ViA7 (Applied Biosystems), using SYBR™ Green as previously described. All expression values were normalized against input DNA and IgG or H3.

### **ModSpec Analysis of Histone Marks**

Histones were acid extracted, derivatized via propionylation, digested with trypsin, newly formed N-termini were propionylated as previously described (Garcia et al., 2007), and then measured 3 separate times using the Thermo Scientific TSQ Quantum Ultra mass spectrometer coupled with an UltiMate 3000 Dionex nano-liquid chromatography system. The data was quantified using Skyline (MacLean et al., 2010), and represents the percent of each modification within the total pool of that tryptic peptide.

### **Cell line cultures**

Cells were seeded at an appropriate density in T 175 cm<sup>2</sup> flasks and incubated at 37°C in the presence of 5 % carbon dioxide. Cells were passaged upon growth to 80-90 % confluence. Cells were treated with trypsin, and then centrifuged to generate a cell pellet. Pellets were re-suspended in an appropriate volume of media before being counted either manually through the use of a haemocytometer or electronically via the Countess II FL Automated Cell Counter (Invitrogen). The viability was measured by staining an aliquot of the cells with Trypan blue (Invitrogen).

### **Proliferation assay**

To assess the proliferative capability, CellTiter-Glo® Luminescent Cell Viability Assay (Promega) was used. Briefly every 24 hours 25 µl of solution was added directly to the media. The fluorescence was measured using FLUOstar Omega (BMG Labtech) plate reader. All measurements were taken in quadruplicate/ quintuplicate.

### **Protein extraction and quantification**

Proteins from cell lines were extracted from 1x10<sup>6</sup> cells, using NE-PER or Subcellular Protein Fractionation Kit for Cultured Cells (PIERCE). Proteins from patients were extracted using 30 µg of frozen tissue using Subcellular Protein Fractionation Kit for tissue with small modification; briefly tissue was washed twice with cold PBS and disrupted in CEB plus protein inhibitors using TissueLyser

II (Qiagen) (3 min/30 oscillation per minutes), the lysated tissue was filtered using 70 µm cell filter (BD) and spun down 300xg for 1 minute.

Proteins extracted were quantified using the BCATM Protein Assay Kit (Pierce) according to the manufacturer's instructions. The samples were incubated at 60°C for 30 minutes, the absorbance of the protein solutions were measured at 562 nm using FLUOstar Omega (BMG Labtech) plate reader.

### **Protein electrophoresis and blotting**

Loading buffer (Lane Marker Reducing Sample Buffer Thermo-Scientific) was added to 5 µg or 1 µg of nuclear or chromatin protein respectively and the sample denatured at 95° C for 5 min, spun briefly and kept on ice. The samples and a molecular weight marker (Spectra Multicolor Broad Range Protein Ladder, Invitrogen) were loaded in a 4-20 % polyacrylamide Amersham ECL Gel (GE Healthcare, UK). The run was performed at a constant 160 mV in Tris – Glycine Running Buffer. The electrophoresed proteins were transferred to a nitrocellulose membrane (Pierce) in a Tris-Glycine-Ethanol Transfer Buffer, by application of an electrical field of 100 mV for 45 min. Then they were incubated in blocking solution.

The membrane was incubated in a solution composed of primary antibodies in T-TBS (BAF47 1:1000, 612110 BD Biosciences; SMARCA4 1:1000, sc-10760 SantaCruz , H3K27me3 1:20000, C15410196 Diagenode; H3K27ac 1:20000, C15410196 Diagenode; H3 1:20000, ab1791 Abcam; B- actin:20000, ab49900 Abcam; Anti-Mouse IgG 1:10000, ab6728 Abcam; Anti-Rabbit IgG 1:10000, ab205718 Abcam; ) for 1 hour at room temperature. It was washed three times in a solution of T-TBS then incubated in a diluted specific secondary antibody (1:10000) for 1 hour at room temperature and washed in T-TBS as before. The blot was developed using SuperSignal West Pico Chemiluminescent Substrate (Pierce) and imaged using ChemiDoc XRS+ (Biorad).

### **DNA/RNA extraction, purification, RNA quantification and quality assessment**

RNA was extracted from pellets of  $1 \times 10^6$  cells using the ZymoBIOMICS DNA/RNA Miniprep Kit (Zymo). RNA samples were stored at -80 °C. RNA quality and quantity was assessed by Bioanalyzer (Agilent Technologies), using Agilent RNA 6000 Nano Kit respectively, following the manufactures procedure.

### **Oligonucleotides**

All oligonucleotides were synthesized by Sigma Aldrich and re-suspended in nuclease free H<sub>2</sub>O (Invitrogen) to a concentration of 100 µmol/µl. Primers for q-PCR were designed using Primer3Plus software (version 4.0.0 and previously; <http://www.bioinformatics.nl/cgi-bin/primer3plus/primer3plus.cgi/>). The transcript sequences of genes were extrapolated from Ensembl (<http://www.ensembl.org/index.html>). The primers were checked for non-specific product using UCSC In-Silico PCR software (<https://genome.ucsc.edu/>).

### **RT-qPCR**

A total of 1000 ng of RNA was converted into cDNA using High-Capacity RNA-to-cDNA Kit (Applied Biosystems) in accordance with the manufacturer's instructions.

The cDNA was amplified using the Platinum SYBR Green qPCR Supermix – UDG with ROX kit (Invitrogen, USA) using ViiA7 machine (Applied Biosystems, UK). The master mix provided is composed of AmpliTaq® DNA Polymerase and SYBR® Green cyanine dye, which as a result of binding to DNA absorbs blue light ( $\lambda_{\text{max}} = 497 \text{ nm}$ ) and emits green light ( $\lambda_{\text{max}} = 520 \text{ nm}$ ). General reaction conditions are shown below.

We quantified the gene expression data using the  $\Delta\Delta\text{CT}$  method. The relative quantification measures the relative change in mRNA expression levels of a gene by comparing to the levels of another RNA. This method does not require a calibration curve and the gene expression is compared against a reference gene. In this study we chose as reference gene *GAPDH*, an endogenously expressed gene.

The gene expression has been calculated following specifically  $\Delta\Delta\text{CT}$  which assumes that each PCR cycle will doubles the amount of amplicons in the reaction (amplification efficiency = 100%) (Livak and Schmittgen, 2001). The fold change expression values have been calculated using this formula: *Fold change expression* =  $2^{-\Delta\Delta\text{Ct}}$  where  $\Delta\Delta\text{Ct} = [\Delta\text{Ct sample1} - \Delta\text{Ct sample2}]$  and  $\Delta\text{Ct} = [\text{Ct sample} - \text{Ct endogenous control}]$ .

### Lentiviral Production and Infection

For Lentiviral particle production,  $3.5 \times 10^6$  HEK293T cells were co-transfected with 7.5  $\mu\text{g}$  of expression vector and the packaging vectors 6  $\mu\text{g}$  of psPax2 and 1.8  $\mu\text{g}$  pVSVg using Calcium Phosphate Transfection (CalPhos Transfection Kits, Clontech). Between twelve hours and fifteen hours after transfection, fresh media was added. Forty-eight hours after transfection, supernatant was collected and concentrated by ultrafiltration in Centricon Plus 100 (Millipore). Particles were aliquoted and stored at  $-80^\circ\text{C}$ .

### Stable lentiviral infection of rhabdoid cells

Lentiviral infection of rhabdoid cells was carried out aiming to transduce about 60%-80% of the total amount of cells in each experiment. Briefly, Viral particles (Multiplicity of infection of 10 and 5; SMARCB1+ and SMARCA4 respectively) were directly added to the media and the cells were incubated for 24 hours at  $37^\circ\text{C}$  and 5%  $\text{CO}_2$ . To select for infected cells, Puromycin (Invitrogen) was added to the media to the final concentration of 1  $\mu\text{g}/\text{mL}$ . The selection was prolonged up to 5 days (*SMARCA4 k/d*) or 7 days (*SMARCB1* stable infection) post-infection, when cells were harvested.

### Plasmids

The self-inactivating, CMV-derived, lentiviral vector pCDH-CMV-MCS-EF1-Puro was purchased from System BioScience. PCDH-CMV-MCS-EF1-Puro contains Ampicillin resistant gene for selection of the plasmid in *E.coli* and Puromycin-resistant marker for selection of the transfected/transduced cells. *pBABE BRG1 dominant negative and shRNA* pBABE BRG1 (K->R) were purchased from Addgene (plasmid 1960). Propagation of all the vectors (excluded pSIN-SIEW) was conducted in the *E. coli* strain DH5 $\alpha$ .

In order to transfect the human cell lines through the lentivirus technology, *BRG1* sequence has been cloned in the suitable pCDH-CMV-MCS-EF1-Puro expression vector. Lentiviral shRNA clones in the

pLKO.1-puro vector were obtained from Sigma-Aldrich TRCN0000015551 (CCGGCCGAGGTCTGATAGTGAAGAACTCGAGTTCTTCACTATCAGACCTCGGTTTTT) TRCN0000015552 (CCGGCCGCGAGACACTGTGATCATTCTCGAGAAATGATCACAGTGTCTGCCGTTTTT); pLKO.1-puro empty vector (Sigma-Aldrich) was used as control.

### **Cell cycle analysis**

Cell cycle stages were determined by measuring the cellular DNA content using flow cytometry. Cells were harvested, washed twice with PBS and fixed with 70% cold ethanol overnight at 4 °C. For cell cycle analysis, the cells were washed twice with cold PBS and centrifuged at 800 rpm for 5 minutes. The cells then were incubated with 100 µg/ml ribonuclease A, RNase (Sigma Aldrich) for 5 minutes followed by 30 minutes staining with 50 µg/ml propidium iodide, PI (Sigma Aldrich). Samples were analysed using a FACSCanto (BD Biosciences) and FlowJo software.

### **Cell senescence analysis**

To determine senescence following *SMARCA4* knockdown and *SMARCB1* reexpression, MRT cells were seeded at a density of  $1 \times 10^5$  in 6-well plate (Corning) and after 5 days or 7 days post-infection respectively,  $\beta$ -galactosidase was measured using senescence detection kit (Sigma Aldrich) according to manufacturer's protocols.

### **EZH2 knock-down and RNA-seq**

For inducible expression of shRNAs, the pINDUCER10 vector (Meerbrey et al., 2011) was obtained from Addgene and linearized with XhoI/EcoRI double digestion. The sequences for targeting EZH2 were obtained from the RNAi consortium (EZH2-2: TRCN0000286290, EZH2-3: TRCN0000293738) and have been previously validated in (Kim et al., 2015), and the sequence for the control (non-targeting) shRNA was obtained from (Sarbasov et al., 2005). The short-hairpin sequences were modified to generate a mir30-based hairpin using the shRNA retriever tool (<http://katahdin.mssm.edu/siRNA/RNAi.cgi?type=shRNA>). Oligos were obtained from IDT, annealed according to manufacturer's instructions and ligated into pINDUCER10.

BT16 cells were grown, selected and maintained at all times in McCoy's 5A medium supplemented with 10% Tet-free FBS (Clontech, cat # 631106), 1% Glutamax.  $2 \times 10^5$  BT16 cells stably expressing either shCTRL or shEZH2-3 were seeded in 6-well plates in triplicates. The next day (d0), fresh medium plus 5 µg/mL doxycycline (Clontech, Cat # 631311 ) was added and after 72 h, RNA was extracted using Trizol and the DirectZol Mini Prep Plu Kit (Zymo research, cat # R2070).

RNA was quantified using the Quant-iT RiboGreen assay (Life Technologies) and quality checked by 2100 Bioanalyzer RNA 6000 Nano assay (Agilent) or LabChip RNA Pico Sensitivity assay (PerkinElmer) prior to library generation. Libraries were prepared from total RNA with the TruSeq Stranded mRNA Library Prep Kit according to the manufacturer's instructions (Illumina.) libraries were analyzed for insert size distribution on a 2100 BioAnalyzer High Sensitivity kit (Agilent Technologies) or Caliper LabChip GX DNA High Sensitivity Reagent Kit (PerkinElmer.) Libraries were quantified using the Quant-iT PicoGreen ds DNA assay (Life Technologies) or low pass sequencing with a MiSeq nano kit (Illumina.) One hundred cycle paired end sequencing was performed on a NovaSeq 6000 (Illumina.)

RNAseq reads were mapped to human GRCh37-lite reference genome by STAR (Dobin et al., 2013). Gene level counts were quantified by HT-seq (Anders et al., 2015) against GENCODE annotation. Read counts were further normalized using TMM(trimmed mean of M values) (Robinson and Oshlack, 2010) methods from R package “EdgeR”. Differential gene expression analysis was performed by R package “limma” (voom function) (Law et al., 2014). The gene were considered differentially expressed if adjusted p value is lower than 0.05 and the fold change is higher than 2. The gene ontology and KEGG pathway enrichment analyses were performed by R function goana and kegg from limma package.

### **Genomic coordinates and gene annotation**

All coordinates used in this study are based on human reference genome assembly hg19, GRCh37 (<http://www.ncbi.nlm.nih.gov/assembly/2758/>). Gene annotations are based on gencode annotation release 19 (<http://www.gencodegenes.org/releases/19.html>).

### **Quantification of gene expression generated by RNA-seq**

Gene expression values in RPKM either for ATRT (Johann et al., 2016) or pediatric normal brain (Roadmap Epigenomics et al., 2015) were quantified using “qCount” function of Bioconductor package quasR (Gaidatzis et al., 2015). Pediatric normal brain RNA-seq data for the two samples HuFNSC01 and HuFNSC02 was obtained from [http://www.genboree.org/EdaccData/Current-Release/sample-experiment/Fetal\\_Brain/mRNA-Seq/](http://www.genboree.org/EdaccData/Current-Release/sample-experiment/Fetal_Brain/mRNA-Seq/).

### **Chromatin segmentation**

18-state Roadmap chromatin segmentation model (Roadmap Epigenomics et al., 2015), which was downloaded from [http://egg2.wustl.edu/roadmap/data/byFileType/chromhmmSegmentations/ChmmModels/core\\_K27ac/jointModel/final/](http://egg2.wustl.edu/roadmap/data/byFileType/chromhmmSegmentations/ChmmModels/core_K27ac/jointModel/final/) (file named as model\_18\_core\_K27ac.txt) was applied on ATRT histone modification ChIP-seq data. The data in bed format (generated using bamToBed function of bedtools (Quinlan and Hall, 2010)) was binarized and subsequently segmented using “BinarizeBed” and “MakeSegmentation” commands of the chromHMM tool (Ernst and Kellis, 2012). Binarization was done using default values. Genomic DNA controls were utilized as background in the identification of binarization thresholds. In the segmentation step, the downloaded Roadmap model (model\_18\_core\_K27ac.txt) was used. This resulted in the chromatin segmentation of 11 ATRTs. Subsequently, “MakeBrowserFiles” command from the chromHMM tool (Ernst and Kellis, 2012) was used to generate segmentation files suitable for UCSC genome browser (Kent et al., 2002) visualization.

### **Multi-track representation of the data**

For each histone ChIP-seq bam file, bigWig files were generated using bamCoverage function of deepTools (Ramirez et al., 2014) with rpkm as the normalization option. Track hubs were constituted for each ATRT separately and were visualized in UCSC genome browser (Kent et al., 2002) using a smoothing window of three pixels.

### **Comparison of chromatin state distributions**

Chromatin segmentations for all Roadmap tissues and cell lines where 18-state chromatin segmentation was available were downloaded from [http://egg2.wustl.edu/roadmap/data/byFileType/chromhmmSegmentations/ChmmModels/core\\_K27ac/jointModel/final/STATEBYLINE/](http://egg2.wustl.edu/roadmap/data/byFileType/chromhmmSegmentations/ChmmModels/core_K27ac/jointModel/final/STATEBYLINE/). Chromatin segmentations for MB (n=23) and GBM (n=3), and pediatric normal brain (n=1) were done using the 18-state chromatin segmentation manner similar to ATRT. The coverage of each chromatin state in the genome was calculated in ATRT, MB, GBM, pediatric normal brain, adult brain (Roadmap) and ESC (Roadmap), and the resulting distributions were represented as boxplots (Figure 1B-1G, Figure S1A). In Figure 1B-1G, after performing ANOVA, pairwise t-test comparisons were performed and adjusted p values were obtained using Benjamini-Hochberg procedure.

### **DNA methylation analysis**

Genomic regions with ReprPC state in PNB were analyzed for the corresponding chromatin states in ATRT subgroups (Figure S2A). To call a 200 bp window to be in a certain chromatin state within an ATRT subgroup, it was required that at least 50% of the samples from the respective subgroup should be in the state under question. Subsequently, the genomic regions with ReprPC state in pediatric normal brain were divided into two groups as “the regions with ReprPC state only in pediatric normal brain” and “the regions with ReprPC state both in ATRT subgroup and pediatric normal brain”. For the resulting genomic regions, DNA methylation values (Figure S2C) were calculated for each ATRT subgroup.

### **Regions losing and gaining H3K27ac/H3K27me3**

Genome was tiled into 2kb windows and H3K27ac and H3K27me3 signals were quantified in BT16 and BT12 ATRT cell lines before and after SMARCB1 re-expression. Genomic regions which were found to have log<sub>2</sub> fold change of 0.5 and -0.5 after SMARCB1 re-expression were referred as the genomic regions gaining and losing the histone modifications, respectively (Figure 2B-2C, Figure S3G-S3H).

### **Representation of the genomic regions**

Genome was classified into regions as exon, intron, intergenic and promoter (region surrounding  $\pm 1$  kb transcriptional start sites) with the hierarchy: promoter > exon > intron > intergenic. Subsequently, each region was intersected with the genomic regions gaining or losing H3K27ac in BT16 and BT12 cell lines (Figure 2D-2E).

### **Peak finding**

Peak finding for SMARCB1 and SMARCA4 was performed using MACS (Zhang et al., 2008) with default parameters.



### **SMARCB1 binding at different chromatin states**

For each of 18 chromatin states, the number of 200 bp bins which are in the respective chromatin state and falling into SMARCB1 peaks were counted in all ATRTs and pediatric normal brain. To evaluate the enrichment of chromatin states at SMARCB1 bound regions, chromatin state frequencies at SMARCB1 bound regions were compared to the ones observed at random genomic regions. Random genomic regions with the same size, number and genomic distribution as SMARCB1 peaks (same exonic, intronic, intergenic, promoter coverage) were created using shuffle command from bedtools (Quinlan and Hall, 2010). Subsequently, for the resulting random genomic regions, the number of 200 bp bins in each chromatin state was calculated in ATRTs and PNB similarly to the calculation performed for SMARCB1 peaks. The resulting values for each chromatin state (arising from the calculation on SMARCB1 peak regions and random regions) were used to build contingency tables, apply Fisher's exact test and calculate the odd ratios. In Figure S4A, chromatin state frequency counts averaged per subgroup were used to compare the counts at SMARCB1 peaks and random regions and apply Fisher's exact test. Figure 3A, chromatin state frequency counts averaged across all ATRTs were used to perform the Fisher's exact test in comparison of SMARCB1 peak regions with random regions.

### **Chromatin states of the promoters bound by SMARCB1**

First, the genomic regions overlapping SMARCB1 binding sites which are in one of TssA, TssFlnkU, EnhG2, EnhA1, and EnhA2 chromatin states in pediatric normal brain were identified. For each subgroup, resulting regions were overlapped with the genomic regions falling into  $\pm 2$  kb surrounding transcriptional start sites and in one of TssBiv, EnhBiv, ReprPC, ReprPCWk and Quies chromatin states in the respective subgroup (to call a genomic region to be in a certain chromatin state, it was required that at least 50% of the samples from the respective subgroup should have the state). Genes with  $\pm 2$  kb surrounding transcriptional start sites satisfying this criteria in all ATRT subgroups were defined as the class of promoters "SMARCB1 bound and active in pediatric normal brain, and switched to repressed chromatin states in ATRT". Resulting set of genes/promoters were used in the comparison H3K27ac and H3K27me3 signal in ATRT vs pediatric normal brain (Figure 3B), pathway enrichment analysis (Figure 3C) and the comparison of the gene expression between ATRT and pediatric normal brain (Figure S4B).

### **Transcription factor motif finding**

"findMotifs" command of the HOMER software (Heinz et al., 2010) were utilized to perform the motif finding. To find the motifs enriched in the promoter regions bound by SMARCB1 and switched to repressed chromatin states in ATRT, regions of the respective promoter overlapping SMARCB1 peaks were used (Figure 4C).

### **Promoters according to EZH2 and H3K27me3 status**

Initially, EZH2 and H3K27me3 signal intensities at promoter regions ( $\pm 1$ kb surrounding TSS) were calculated in rpkm using the functions described in (Hisano et al., 2013). For both EZH2 and H3K27me3, a single intensity value per promoter was obtained by taking the average over all ATRTs. Resulting values were modelled by fitting two normal distributions to the data using the R package 'mclust' (<http://www.stat.washington.edu/mclust>). Using a p value cut-off of 0.0001, thresholds for



being H3K27me3-positive and EZH2-positive were determined as 0.931 and 0.780, respectively (Figure S5A-S5B). Subsequently, these thresholds were used to determine EZH2<sup>+</sup> and H3K27me3<sup>+</sup> promoters in each subgroup simply by checking which promoters have a subgroup average signal value greater or equal to the thresholds determined. Figure S5C-S5E show the comparison of EZH2 and H3K27me3 in scatter plots for the three ATRT subgroups and thresholds were shown as dashed red lines. In Figure 4A, “Bound by EZH2” status refers to being EZH2 positive according to the cut-offs identified (Figure S5A-S5B) in all ATRT subgroups. Figure 5A displays EZH2<sup>+</sup>/H3K27me3<sup>-</sup> or EZH2<sup>+</sup>/H3K27me3<sup>+</sup> promoters in all ATRTs irrespective of the subgroup. With similar usage of mclust package and using a p value cut-off of 0.001, H3K27me3-positive and EZH2-positive promoters were also defined for PNB (Figure S5G) and hESCs (Figure S5H).

### Chromatin states at different EZH2/H3K27me3 classes

For each promoter class from EZH2<sup>+</sup>/H3K27me3<sup>-</sup> or EZH2<sup>+</sup>/H3K27me3<sup>+</sup>, the chromatin state of the each 200 bp genomic bin falling into the  $\pm$  5kb Tss region was determined in ATRTs. The assignment of the chromatin state was performed using the chromatin state with the maximum representation among all ATRTs. The results were displayed as heatmaps (Figure 5D).

### Plotting ChIP-seq signal around TSS

To quantify ChIP-seq signal around transcriptional start sites of the genes “*profilesForRegions*” function was used as described (Hisano et al., 2013). To summarize, the read counts at each position within  $\pm$  2kb Tss regions (Figure 3B) were summed and averaged over 50 bp windows tiling the region. Resulting values were scaled to a range between 0-1 and plotted as heatmaps. In Figure 3B, to plot H3K27ac and H3K27me3 signals in ATRT, signal intensities were averaged across all ATRTs. Regarding the display of EZH2, SUZ12, SMARCA4 and H3K27me3 signals at different EZH2/H3K27me3 promoter classes for ATRT-TYR, ATRT-SHH and ATRT-MYC (Figure S6), each ChIP-seq signal was averaged across the samples from the same subgroup. In order to create the heatmaps in Figure 6A-6B, ChIP-seq signals from all ATRTs were averaged irrespective of the subgroup.

### Pathway enrichment analysis

Functional annotation of the genes with promoter regions bound by SMARCB1 and switched to repressed chromatin states in ATRT (Figure 3C) was performed using ClueGO plugin for Cytoscape (Bindea et al., 2009) and using GO (Biological process, levels 8-15), KEGG, Reactome and Wiki pathways. Enriched pathways were determined using the following settings: go-term fusion option, p value threshold of 0.05 and other parameters as default. The output associated with only a single gene set was manually discarded.

## QUANTIFICATION AND STATISTICAL ANALYSES

All meta analysis performed using bam files and statistical analyses were performed using R and bioconductor packages. Basic quantification of ChIP-seq data was performed using the functions “coverageForChr”, “countsForRegions” and “profilesForRegions” described in (Hisano et al., 2013). Quantification of published RNA-seq was done using “qCount” function of Bioconductor package quasR (Gaidatzis et al., 2015). ANOVA, and pairwise t-test comparisons to compare the chromatin

state distributions across different tissue types (Figure 1); Fisher's exact test to show differential representation of SMARCB1 binding sites at chromatin states (Figure 3) were performed in R. Analysis of differential representation of cell cycle phases, RT-qPCR and ChIP-qPCR after SMARCA4 knock-down in BT12 and BT16 were carried out using 2 way- ANOVA in (Figure 7).

#### **DATA AND SOFTWARE AVAILABILITY**

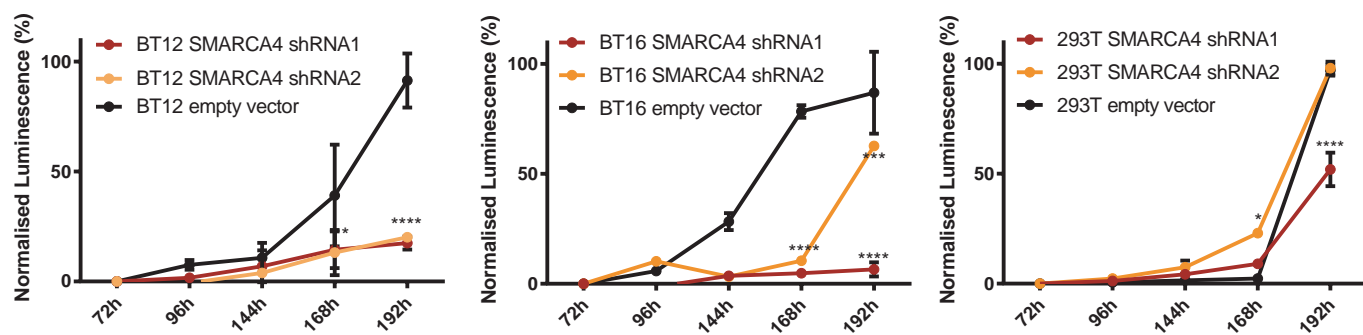
Short-read sequencing data have been deposited at the European Genome-Phenome Archive (EGA, <http://www.ebi.ac.uk/ega/>) hosted by the EBI, under accession number EGAS00001001297 with dataset group number EGAD00001003408.

Table S1. Related to Figure 1. List of samples included in the study, including their subgroup affiliation, and generated ChIP-seq data availability.

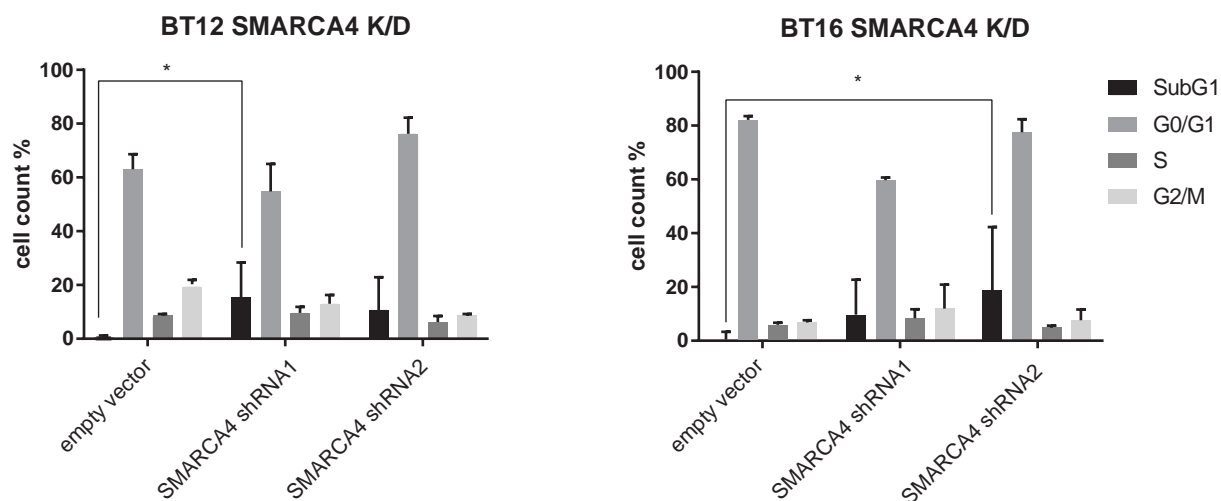
Table S2. Related to Figure 3. List of genes and their  $\pm$  2kb TSS regions, bound by SMARCB1 and active in PNB but associated with repressed chromatin states in ATRT (referring to Figure 3B).

Table S3. Related to Figure 5. Promoters with upper 5th percentile EZH2 enrichments in ATRT, which are in EZH2+/H3K27me3- status. Table S3A shows the genes and promoter coordinates and TableS3B shows the pathways associated with the genes (Output of ClueGo pathway enrichment analysis).

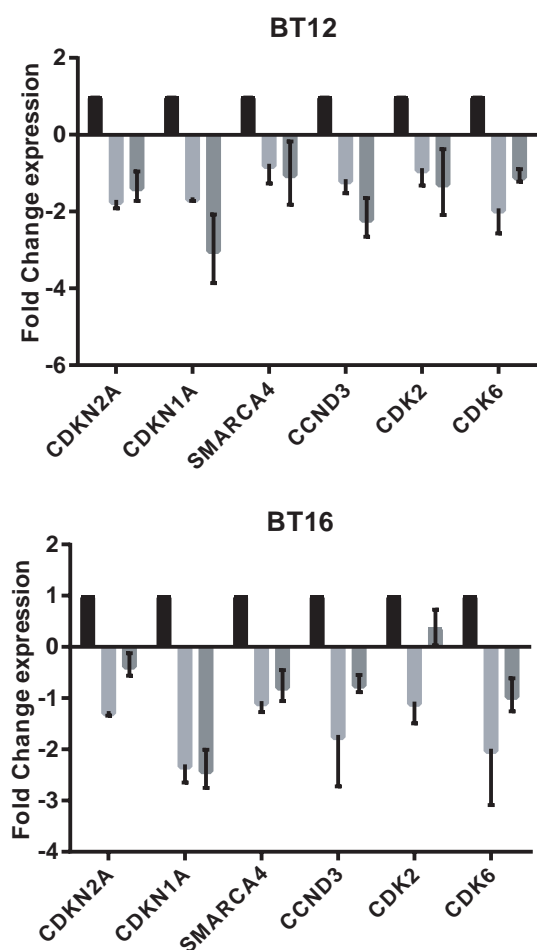
**A**



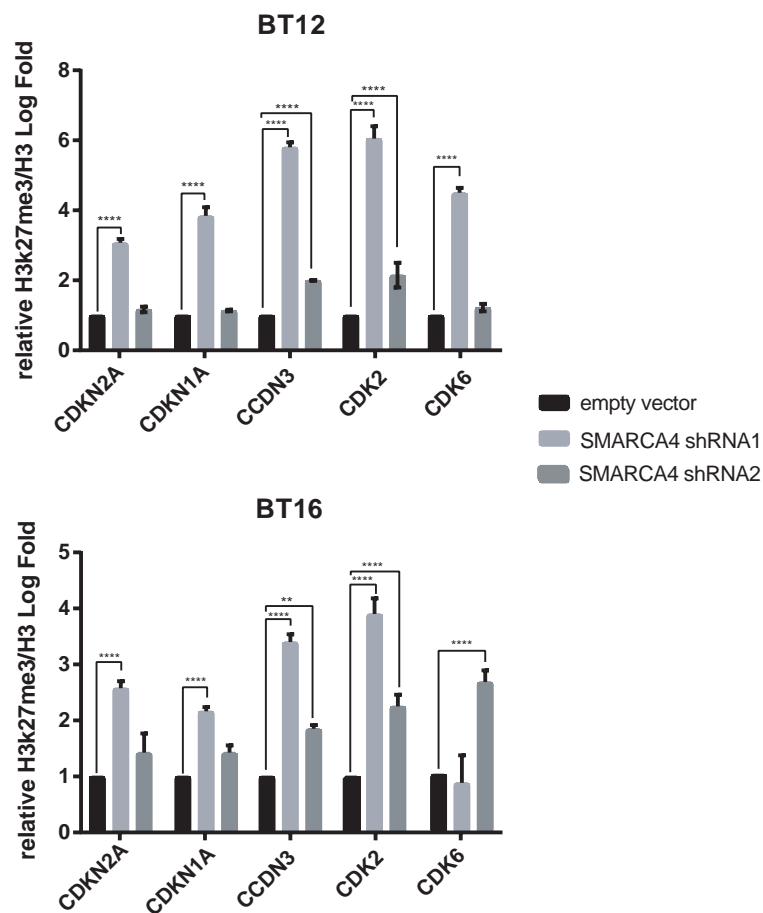
**B**



**C**

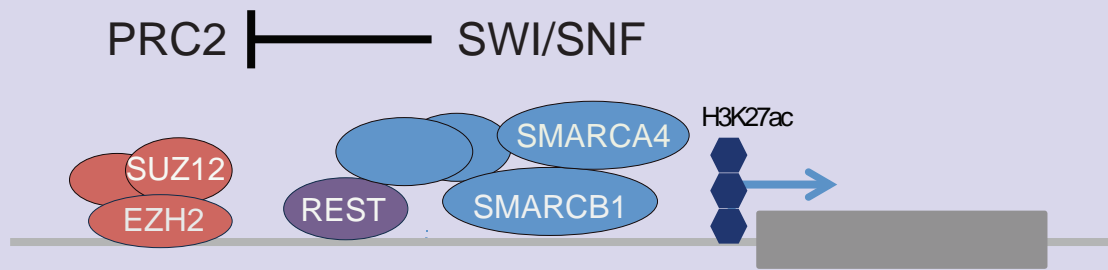


**D**



## Normal brain

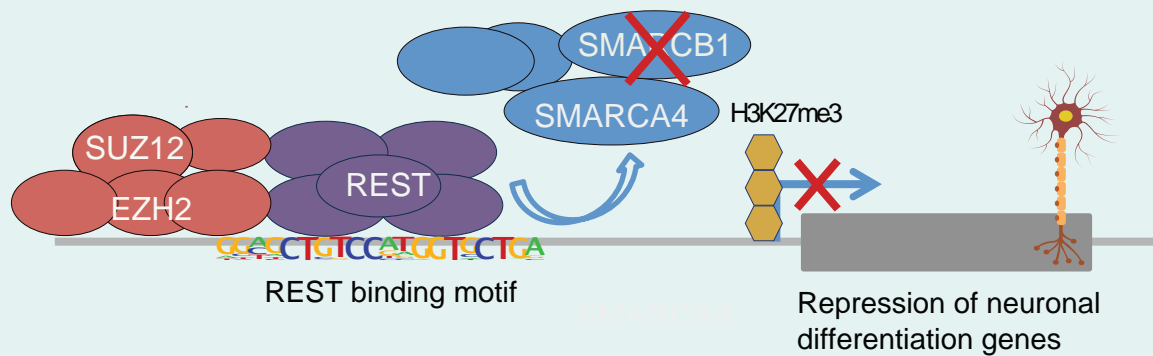
SWI/SNF inhibits PRC2 mediated repression and genes are actively expressed despite the presence of REST and the PRC2 complex.



## ATRT

EZH2<sup>+</sup>/H3K27me3<sup>+</sup> genes

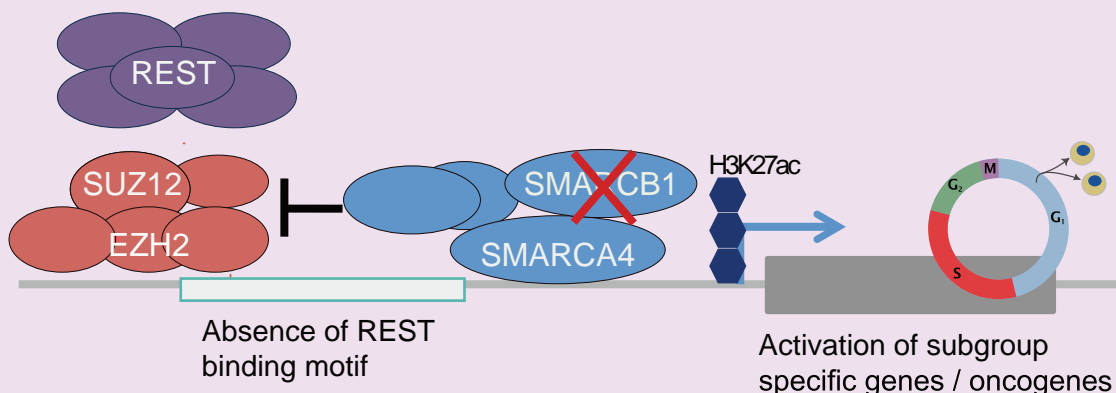
Loss of SMARCB1 leads to disassembly/displacement of SWI/SNF. Thus inhibition of PRC2 is lost and - in concert with other factors such as REST - it is able to repress e.g. tumor suppressor genes and neuronal differentiation genes, where the REST binding motif is present.



## ATRT

EZH2<sup>+</sup>/H3K27me3<sup>-</sup> genes

Loss of SMARCB1 does not lead to displacement of SWI/SNF at all genes. Residual SWI/SNF maintains activity of (super)-enhancers, promoters of cycle genes and activated oncogenes. REST binding at these genes is not possible because the binding motif is missing. EZH2 still acts as a repressor at these sites but full activity is inhibited by residual SWI/SNF complex.



## **Supplemental Information**

### **Comprehensive analysis of chromatin states in atypical teratoid/rhabdoid tumor identifies diverging roles for SWI/SNF and Polycomb in gene regulation**

Serap Erkek, Pascal D. Johann, Martina A. Finetti, Yiannis Drosos, Hsien-Chao Chou, Marc Zapatka, Dominik Sturm, David T.W. Jones, Andrey Korshunov, Marina Rhyzova, Stephan Wolf, Jan-Philipp Mallm, Katja Beck, Olaf Witt, Andreas E. Kulozik, Michael C. Frühwald, Paul A. Northcott, Jan O. Korbel, Peter Lichter, Roland Eils, Amar Gajjar, Charles W.M. Roberts, Daniel Williamson, Martin Hasselblatt, Lukas Chavez, Stefan M. Pfister, Marcel Kool

**Figure S1. Related to Figure 1. Distribution of the chromatin states in ATRT.**

**(A)** Boxplots show the coverage of each chromatin state across ATRT subgroups, GBM, MB, ANB, PNB, and ESC.

**(B-C)** Boxplots show the H3K27ac (B) and H3K27me3 (C) levels at 10kb windows tiling the genome in ATRT and PNB. For the comparisons, 10kb windows with min 1 rpkm value either in ATRT or PNB were taken into account. \*Wilcoxon test p-value < 2.2e-16.

**(D-E)** Boxplots show the H3K27ac (D) and H3K27me3 (E) levels at 10kb windows tiling the genome in ATRT and MB. For the comparisons, 10kb windows with min 1 rpkm value either in ATRT or MB were taken into account. \*Wilcoxon test p-value < 2.2e-16.

**(F)** Mass spectrometry analysis shows the H3K27ac (left panel) and H3K27me3 (right panel) levels in ATRT and MB.

**Figure S2. Related to Figure 1. Polycomb repressed regions in PNB largely lack H3K27me3 and have increased DNA methylation in ATRT.**

**(A)** Pie-charts display the corresponding chromatin states in ATRT subgroups for the genomic regions that are in ReprPC state in PNB. For visualization purposes, the representations of some of the chromatin states were combined as indicated.

**(B)** Snapshots show the H3K27me3 signal at selected genomic regions in PNB and ATRT subgroups. For ATRT subgroups, H3K27me3 data is a multilayer overlay representing the samples from each subgroup.

**(C)** Boxplots show the average percentage of DNA methylation in ATRT subgroups at genomic regions with ReprPC state both in PNB and in one of ATRT subgroups (dark colors) and the genomic regions with ReprPC state in PNB only (light colors). \*Wilcoxon test p-value < 2.2e-16.

**Figure S3. Related to Figure 2. Phenotypic and H3K27me3 profiles in BT12 and BT16 ATRT cell lines after SMARCB1 re-expression.**

**(A)** Protein simple WES system analysis confirming SMARCB1 re-expression in BT12 and BT16 cell lines at 7th day post transfection; 293t is positive control; B-actin was used as loading control.

**(B)** Images of BT12 and BT16 before and after re-expression of SMARCB1.

**(C)** Growth curve (Luminescent Assay) over 7 days showing growth arrest in BT12 and BT16 following SMARCB1 re-expression; mean of triplicates error bars represents standard deviation.

**(D)** SMARCB1 stable re-expression causes suppression of colony formation BT12 and BT16 cells. 7 days post transfection, colonies were stained and plates were photographed.

**(E)** SMARCB1 re-expression induces senescence. Evaluation of  $\beta$ -galactosidase activity in BT16 and BT12 at 7th post infection. Senescent cells are stained blue.

**(F)** Cell cycle analysis using propidium iodide (PI) staining and flow cytometry at 3rd and 5th day post infection. Results are the mean  $\pm$  SE of two separate experiments. 2 way Anova analysis was used to test the significant difference between each group and the empty vector control are shown as  $p \leq 0.01$  (\*);  $p \leq 0.001$  (\*\*),  $p \leq 0.001$  (\*\*\*) and  $p \leq 0.0001$  (\*\*\*\*).

**(G-H)** MA plots (left) show the comparison of the average H3K27me3 levels and log2 fold changes after SMARCB1 re-expression for BT12 (G) and BT16 (H) in 2kb windows tiling the genome.

**(I)** Mass spectrometry analysis showing the percent change in H3K27ac and H3K27me3 levels after re-expression of SMARCB1 in BT12 and BT16 cell lines. Error bars show the standard deviation of three replicates.

**(J)** Snapshots show H3K27ac profiles before and after re-expression of SMARCB1 in BT12 and BT16 cell lines at UNC5C, NDRG1 and NEDD4L loci. Barplots next to the snapshots show the average log2 fold changes of expression after SMARCB1 re-expression for the respective genes in BT12 and BT16.



**Figure S4. Related to Figure 3. Chromatin states at SMARCB1 binding sites in ATRT subgroups.**

**(A)** Heatmap display the observed over expected chromatin state frequencies at SMARCB1 binding sites in ATRT subgroups (See STAR Methods for details).

**(B)** Boxplot shows the mean expression level of the genes from Figure 3C in ATRT and PNB confirming the predicted transcriptional repression in ATRTs. Wilcoxon test p-value=8.5e-48.

**(C)** Contingency table built to test the enrichment of tumor suppressor genes (TSG) among genes bound by SMARCB1 in PNB and switched to repressed chromatin states in ATRT. Fisher's Exact Test p-value=0.01272.

**(D)** Snapshot (left panel) displays the PNB SMARCB1 signal and the chromatin segmentations in PNB (n=1) and ATRT subgroups (TYR, n=5, SHH, n=3, and MYC, n=3) at the *WNK2* locus. The expression level of *WNK2* in ATRT subgroups and PNB is presented as boxplot next to the image.

**Figure S5. Related to Figure 5. Definition of EZH2<sup>+</sup> and H3K27me3<sup>+</sup> promoters and comparison of H3K27me3 and EZH2 in ATRT subgroups and in other entities.**

**(A-B)** Density plots show the distribution of the signal (gray) for EZH2 (A) and H3K27me3 (B) in ATRT, and resulting separation of the signal as foreground (positive for H3K27me3 (A) or EZH2 (B)) (green) and background (negative for H3K27me3 (A) or EZH2 (B)) (blue) at a p value threshold of 0.0001 (red line).

**(C-E)** Scatter plots show the comparison of H3K27me3 and EZH2 at promoter regions of the genes for ATRT-TYR (C), ATRT-SHH (D), ATRT-MYC (E) with red dashed lines depicting the cut-offs for H3K27me3 and EZH2 as identified in (A) and (B).

**(F)** Scatter plot showing the comparison of H3K27me3 and EZH2 at promoter regions of the genes for BT16 (ATRT cell line).

**(G)** Scatter plot showing the comparison of H3K27me3 and EZH2 at promoter regions of the genes for PNB. Red dashed lines depict the cut-offs identified for H3K27me3 (0.771) and EZH2 (1.177) in PNB with the same methodology as in (A) and (B).

**(H)** Scatter plot comparing the H3K27me3 and EZH2 illustrates the largely absence of EZH2<sup>+</sup>/H3K27me3<sup>-</sup> class of promoters in ESC. Red dashed lines depict the cut-offs identified for H3K27me3 (1.011) and EZH2 (2.015) in ESCs with the same methodology as in (A) and (B).

**(I-K)** ChIP-qPCR validations for H3K27me3 (I), SUZ12 (J) and EZH2 (K) at selected loci, RBM14, CDK4, SMARCE1, HDAC2 (EZH2<sup>+</sup> H3K27me3<sup>-</sup>) and NEUROD2 (EZH2<sup>+</sup> H3K27me3<sup>+</sup>) in three ATRTs. ACTB and Untr12 serve as negative controls.

**Figure S6. Related to Figure 6. Residual SWI/SNF occupancy at EZH2<sup>+</sup>/H3K27me3<sup>-</sup> promoters across ATRT subgroups.**

**(A)** Heatmaps (panels on the left) display scaled-read densities for EZH2 (blue), SUZ12 (brown), SMARCA4 (red) and H3K27me3 (dark gray) at regions surrounding  $\pm 2$  kb transcriptional start sites of the genes with EZH2<sup>+</sup>/H3K27me3<sup>-</sup> promoters in ATRT-TYR (upper panel) and with EZH2<sup>+</sup>/H3K27me3<sup>+</sup> promoters in ATRT-TYR. For visualization purposes, 2000 randomly chosen promoters are shown either from EZH2<sup>+</sup>/H3K27me3<sup>-</sup> or EZH2<sup>+</sup>/H3K27me3<sup>+</sup> classes. Scatter plot (middle panel) showing the comparison between average EZH2 in ATRT-TYR and SMARCA4 in ATRT-TYR at promoter regions of the genes. Promoters are colored according to their EZH2/H3K27me3 status in ATRT-TYR. Snapshots displaying the multilayer H3K27ac, H3K27me3, EZH2, SUZ12 and SMARCA4 signals in ATRT-TYR at *BMP4* locus.

**(B-C)** Same as in (A) for ATRT-SHH (B) and ATRT-MYC (C), respectively. Snapshots displaying the multilayer H3K27ac, H3K27me3, EZH2, SUZ12 and SMARCA4 signals in ATRT-SHH at *SOX11* locus (B) and in ATRT-MYC at *MYC* (C) locus, respectively.

**Figure S7. Related to Figure 6. Overlap of SMARCA4 and SMARCB1 co-occupied regions with EZH2<sup>+</sup>/H3K27me3<sup>-</sup> and EZH2<sup>+</sup>/H3K27me3<sup>+</sup> promoters and residual SWI/SNF occupancy at ATRT subgroup specific enhancers.**

**(A-B)** Barplots show the percentage of EZH2<sup>+</sup>/H3K27me3<sup>-</sup> (A) or EZH2<sup>+</sup>/H3K27me3<sup>+</sup> (B) promoters overlapping both SMARCA4 peaks in ATRT and SMARCB1 peaks in PNB. In the analysis, only the SMARCA4 peaks which can be found in at least two ATRTs and having SMARCA4 enrichments in the upper 20<sup>th</sup> percentile were used.

**(C)** Heatmap displaying the scaled-read density for REST at regions surrounding  $\pm 5$  kb TSS of the genes with EZH2 + / H3K27me3 - status. At the top, density plot shows the average signal intensity displayed in the heatmap below.

**(D)** Dose dependent reduction of EZH2 levels upon increased concentration of doxycycline. BT16 shCTRL or shEZH2-3 cells were treated with either 1 or 5  $\mu$ g/mL doxycycline and levels of EZH2, H3K27me3, H3 and ACTIN (loading controls) were determined by western blot after 72h.

**(E)** Volcano plot shows the log2 fold change in gene expression after EZH2 knock-down in BT16 cells vs -log10 (PValue). Genes which are significantly ( $\log_2FC > 1$  and  $FDR < 0.05$ ) downregulated (n=695) and upregulated (n=1151) are shown with a red color.

**(F)** Boxplots show the average H3K27me3 levels in ATRT for upregulated and downregulated genes according to their EZH2/H3K27me3 status. \* Wilcoxon-test p-value  $< 1.0 \times 10^{-9}$ .

**(G)** Barplot shows the overlap of ATRT subgroup specific-enhancers (overlapping and non-overlapping with super-enhancers) with SMARCA4 peaks.

**(H-J)** Scatter plots display the comparison between average EZH2 and SMARCA4 in ATRT-TYR at TYR-specific enhancers (n=2048) (H), in ATRT-SHH at SHH-specific enhancers (n=1126) (I), and in ATRT-MYC at MYC-specific enhancers (n=495) (J). Enhancers contained within super-enhancers are shown in orange/red color.

**(K)** Scatter plot shows the comparison of EZH2 and SMARCB1 at all promoters. Pearson correlation coefficient,  $r=0.88$ .

**(L)** Heatmaps display scaled-read densities for EZH2 (blue), SMARCB1 (red) and H3K27me3 (dark gray) at regions surrounding  $\pm 2$  kb transcriptional start sites of the genes with EZH2<sup>+</sup>/H3K27me3<sup>-</sup> promoters in PNB. EZH2<sup>+</sup>/H3K27me3<sup>-</sup> promoters in PNB were defined (Figure S5G) similarly as in ATRT. For visualization purposes, 2000 randomly chosen promoters are shown from EZH2<sup>+</sup>/H3K27me3<sup>-</sup> class.

**(M)** Protein simple WES system analysis confirming SMARCA4 knock down in BT12 and BT16 cell lines over time (3 days and 7 days post transfection); B-actin was used as loading control.

C

R=0.972

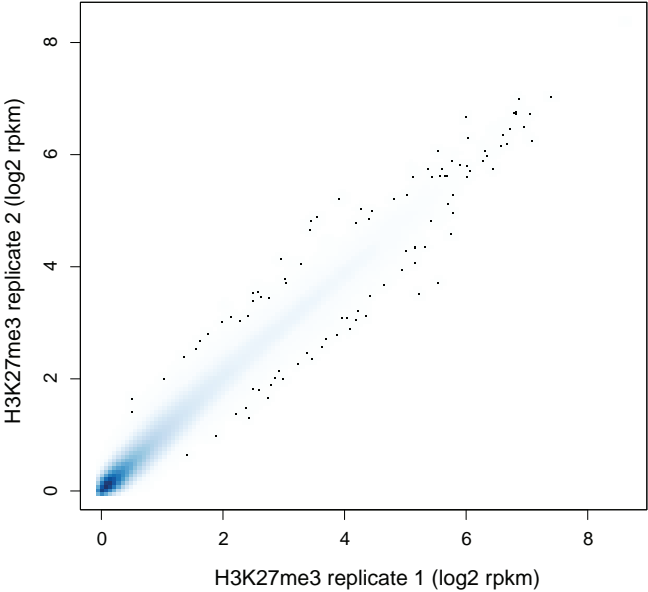


**Figure S8. Related to STAR Methods. Quality metrics for ChIP-seq.**

**(A)** ChIP-qPCR data for one selected ATRT for the histone modifications, H3K4me1 (Untr12: negative control, ACTB In3: positive control), H3K4me3 (Untr12 and Untr4: Negative controls, ACTB -145 and GAPDH pro: positive controls), H3K27me3 (ACTB -145: Negative control, MYT1 -1772, PTGER3 +1149 and CCND2 +47: positive controls), H3K27ac (Untr12 and SNGH8 +1137: negative controls and ACTB -145: positive control), H3K9me3 (Untr12: negative control, ZNF184 +20k and ZNF678 +90k: positive controls) and H3K36me3 (Untr12: negative control, ACTB In3: positive control). Data was generated by from Active Motif. 'Untr' specifies 'untranslated region', 'pro' specifies 'promoter', '+' or '-' specifies the distance from the transcriptional start sites of the genes.

**(B)** Table shows the number of mapped reads for the six histone modifications in ATRT ChIP-seq cohort.

**(C)** Scatter plot shows the correlation between technical replicates of H3K27me3 generated from the same primary ATRT sample at 2kb windows tiling the genome.